FISEVIER

Contents lists available at ScienceDirect

Journal of Computational Physics

journal homepage: www.elsevier.com/locate/jcp





A computational approach to modeling flow-induced large deformation of thin-walled compliant vessels

Oleksander Krul, Prosenjit Bagchi*

Mechanical and Aerospace Engineering Department, Rutgers, The State University of New Jersey, Piscataway, 08854, NJ, USA

ARTICLE INFO

Keywords: Compliant vessels Deformable interface Fluid/structure interaction Immersed-boundary methods Law of Laplace

ABSTRACT

We present a computational method capable of modeling 3D flow-induced deformation of thin, highly compliant, hyperelastic vessels conveying viscous, inertial fluid. The method can uniformly consider vessel extension and collapse. Very large inflation, transient deformation, complex flow features as well as highly complex buckling shapes are well resolved by this method. The methodology combines finite volume and spectral methods for fluid motion, finite element method for structural mechanics of the vessel wall, and the immersed boundary method for twoway coupling between the wall and fluid. A hybrid of the continuous forcing and the ghost node methodologies capitalizing on the strengths of each is developed. The method avoids the surface instability encountered with the continuous forcing methods, as well as the need for domain remeshing as required in the iterative and partitioned approaches. The vessel wall can follow linear or nonlinear (strain softening and hardening) material models, and the fluid inertia can vary over a wide range. We demonstrate the versatility of the method by considering vessel inflation and collapse with large, complex, and transient deformation. Remarkable differences in vessel inflation at low versus moderate inertia are observed; this includes steady versus oscillatory motion, emergence of flow recirculation and pressure wave reflection which are well resolved. For the collapsing vessels, well-defined shapes with different buckling modes as well as highly complex buckling with fine surface folds are predicted. Additionally, a second-order correction to the well-known law of Laplace is developed and used to validate our computational results for vessel inflation.

1. Introduction

Flow through deformable vessels appears in many biological and engineering applications. Most blood vessels are deformable. Large arteries expand during systole and relax during diastole, which mitigates the intermittent flow delivered by the heart [1]. Veins, which contain about 80% of the blood volume in the vascular system, are highly compliant and may collapse at low pressure, leading to the vascular waterfall phenomenon [1]. Smaller arteries and capillary vessels are also compliant; they can dilate and contract either passively, in response to cardiac rhythms, or actively, by the action of smooth muscle cells and nerve cells [1]. Lung airways, lymphatic vessels, and the urinary tract are also deformable. Engineering applications include flexible microfluidics, e.g., microchannels with compliant thin-walled membranes, micropumps, and pressure sensors [2].

https://doi.org/10.1016/j.jcp.2024.113026

Received 26 September 2023; Received in revised form 19 March 2024; Accepted 15 April 2024

Available online 19 April 2024

0021-9991/© 2024 The Author(s). Published by Elsevier Inc. This is an open access article under the CC BY-NC-ND license (http://creativecommons.org/licenses/by-nc-nd/4.0/).

^{*} Corresponding author.

E-mail address: pbagchi@soe.rutgers.edu (P. Bagchi).

Compliant vessels are a fluid/structure interaction (FSI) problem in which the vessel wall and flow are, in the generic case, two-way coupled, and both may exhibit complex, transient behaviors. Theoretical works in this field, which are briefly noted below, have considered simplified analytical models under restrictive conditions in lieu of a complete FSI solution. Several one-dimensional models have been developed to predict steady, axisymmetric flow through an inflating elastic tube with thin walls [1,3,4]. These models assume the flow adheres locally to Poiseuille law, the vessel exhibits small deformation, and the fluid pressure is balanced by the stress in the vessel wall. The pressure-radius relationship was prescribed either via experimental determination [3] or by a model derived from linear elasticity theory, e.g., the Law of Laplace [1], Kirchhoff shell theory, or membrane theory [4]. Notably, these models predict a nonlinear flow rate-pressure drop relationship, unlike that of a rigid vessel. The applicability of these models to moderate deformation has also been considered [4], with further models permitting large deformations of hyperelastic tubes [5]. Other works incorporate fluid inertia, either as an extension of the methods discussed above [6], or through 1D wave models describing the vessel wall motion [7]. Flows in rectangular channels with compliant walls have been similarly modeled [2]. Collapsing tubes have also been extensively studied analytically [8]. An early model by Timoshenko that considered only structural mechanics (i.e., without any fluid motion) predicted different shapes (or modes) of buckling that would occur under a critical load [9]. When fluid motion is considered, flow limitation occurs in response to a rapid decrease in the cross-sectional area over a small change in pressure as the tube buckles. This has been discussed by Pedley & Luo [10] and several other studies [1.8.11]. Several 1D models predicting this complex relationship between transmural pressure and cross-sectional area have been developed [10-13].

Computational methods that treat deformable vessels as a complete fluid-structure interaction problem are nontrivial, requiring a solution of the full Navier-Stokes equations coupled with the structural equations of the vessel wall, which may follow a complex, nonlinear, and viscoelastic response. A common solution method is to use a partitioned solver, where the fluid and structure are solved separately and implicitly coupled through an iterative feedback loop. A series of works from Heil, Pedley, and Hazel follow this approach using a finite element method (FEM) to simulate the steady collapse of a Kirchhoff-Love type elastic tube [14–17]. These works cover solutions for various flow conditions, including viscous and inertial fluid at both low and high Reynold's numbers. This approach has also been applied to collapsing hyperelastic vessels by Zhang et al. with an adaptation of the arbitrary Lagrangian-Eulerian (ALE) FEM [18]. As noted in [19], partitioned, body-conformal FEM approaches such as these can be expensive in some problems because they require frequent remeshing of the computational domain.

For many moving boundary problems, the immersed boundary (IB) methods are a chosen means of solution. The IB methods can enforce fluid boundary conditions on arbitrarily shaped bodies that do not conform to the computational mesh; therefore, they do not require remeshing of the fluid domain [19]. This versatility lends itself well to problems with complex geometries and arbitrary deformations. As such they have been used for deforming vessel problems with varied and complex fluid-structure interactions, including both active or passive (i.e., when the motion is prescribed as known a priori, or found as a solution of the full FSI, respectively) deformation, viscoelastic tube wall mechanics, and viscoelastic fluids [20], [21,22]. In these methods, a body-force term is added to the Navier-Stokes equations that represents the influence of the immersed boundary. IB methods are generally categorized as either a continuous forcing or a direct forcing method, depending upon their treatment of the added force [23]. The former was initially conceived by Peskin to model the flow around heart valves [24,25]. In this approach, the forces generated in the deforming interface are spread to the surrounding fluid through the body-force term, and the interface is advected using the surrounding fluid velocity. This formulation intrinsically models passively deforming, thin structures, which may include complex properties such as nonlinear viscoelasticity and bending resistance [26]. These properties make it suitable for modeling biological flows [27], [28,29], [30], bubbles, drops, red blood cells, vesicles, and capsules [26,31–37]. Extensions to this method, known as penalty IB methods, can model constrained boundary motion, including prescribed deformation [21], fixed boundaries [22], massive boundaries [38], and rigid body motion [19,23,39,40].

In contrast to the continuous forcing method, in the direct forcing methods the force is added after discretizing the governing equations. As was first shown by Mohd-Yusof [41] and Verzicco et al. [42], the force term may then be rewritten to directly impose the desired surface velocity. This creates a "sharp" interface that is second-order accurate in space [23]. Many direct forcing methods have been developed, e.g., cut-cell, ghost-cell, and volume penalization, for different applications, many of which take advantage of the sharp interface to resolve complex geometries [43–45]. Popular among them is a versatile ghost-cell method developed by Mittal [46], which has been used to model intricate systems of vessels, e.g., in capillary vascular networks [35] and cardiac hemodynamics [47,48]. Modeling passive deformation with the direct forcing method requires, in general, the use of an iterative partitioned approach [49]. However, iterations can be avoided in problems which are well described by a one-way coupling, such as in [48], as discussed by Boustani et al. [50]. Additionally, passive rigid body motion can be modeled non-iteratively following a method introduced by Uhlmann [51], which was later modified by Breugem [52].

In this work, we present a generic, non-iterative, fully 3D computational approach for the two-way coupled FSI of flow through deformable, thin-walled vessels. The method can uniformly consider both vessel inflation and collapse. Very large distention, transient deformation, complex flow features, and highly complex buckling shapes can be predicted using this method. The vessel wall can follow either linear or nonlinear material models, and the fluid inertia can vary over a wide range. The methodology combines finite volume and spectral methods for fluid motion, finite element method for structural mechanics, and IBM for two-way coupling. Specifically, we present a hybrid of the continuous forcing and the ghost node methodologies to treat the deforming wall. We then demonstrate the versatility of the method by considering vessel inflation and collapse with large, complex, and transient deformation. Additionally, we present a second-order theory of vessel inflation and validate our computational method against it.

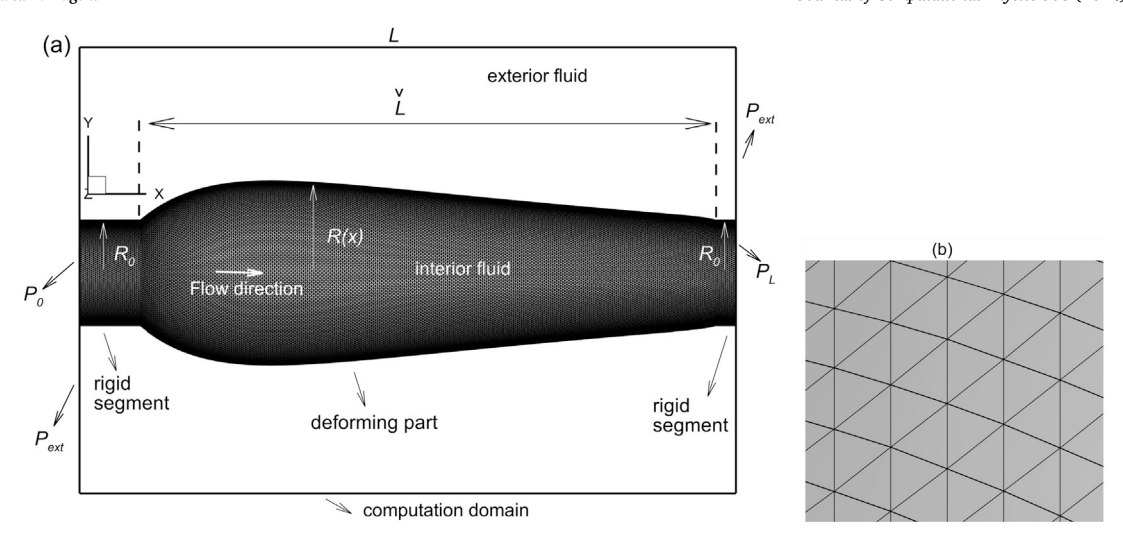


Fig. 1. Problem setup. (a) Vessel, computation domain and some parameters as defined in the text. (b) a close-up of the Lagrangian mesh on the vessel surface.

2. Methodology

2.1. Problem setup

The problem setup is given in Fig. 1(a). The undeformed tube is assumed to have a circular cross-section with radius and total length denoted by R_0 and L. The vessel and fluid motion have two-way (i.e., strong) coupling; the vessel is deformed naturally (i.e., without any prescribed displacement) by the fluid motion, and the flow in turn is affected by the movement of the vessel wall. The streamwise flow direction is x, and x=0 and L are the inlet and outlet, respectively. The vessel is immersed within a rectangular (box-like) computational domain with the inlet and outlet coinciding with the left and right boundaries of the domain. The flow inside the vessel is driven by specifying a pressure P_0 at the inlet and P_L at the outlet. An external pressure P_{ext} is specified over the left and right boundaries of the computational domain outside the tube inlet and outlet. The zero normal derivatives are specified for velocities at the left and right boundaries, while the periodic boundary condition is specified in the z direction, and the zero-velocity condition is enforced at the y boundaries of the computation domain. The fluids interior and exterior to the tube are assumed to have same density ρ and viscosity μ . The tube is divided into three streamwise segments: two rigid segments at the entrance and exit, and a deforming part of length \check{L} in between. The two ends of the deforming segment are thus 'pinned'. The rigid segments allow the flow to adjust for the changes in the deforming section. Additionally, the rigid inlet ensures a fully developed flow enters the deforming part.

2.2. Structural mechanics

The vessel wall in the deforming section is hyperelastic and materially isotropic. The undeformed and deformed states of the vessel are represented by coordinates of a material point as X and x(X,t), respectively. In a general 3D description, the deformation gradient and Green strain tensors are defined as $\mathbf{A} = \frac{\partial x}{\partial X}$ and $\mathbf{E} = \frac{1}{2} \left(\mathbf{A}^T \cdot \mathbf{A} - \mathbf{I} \right)$, respectively, where \mathbf{I} is the identity tensor. The Cauchy stress may then be given as $\sigma = \frac{1}{J}\mathbf{A} \cdot \frac{\partial W}{\partial \mathbf{E}} \cdot \mathbf{A}^T$, where $J = \det{\{\mathbf{A}\}}$ is a measure of volume dilation, and W is the strain energy function, whose form depends on the constitutive model of the material [53,54].

We assume that the vessel wall is thin and neglect stress variation through its thickness, h. Then, the 3D wall mechanics can be recast as a 2D plane stress problem in the tangent plane of the wall. In this form, the surface deformation gradient $\hat{\mathbf{A}}$ and Green strain tensor $\hat{\mathbf{E}}$ are given as [55,56]

$$\hat{\mathbf{A}} = (\mathbf{I} - nn) \cdot \frac{\partial \mathbf{x}}{\partial \mathbf{X}} \cdot (\mathbf{I} - NN), \tag{1}$$

and

$$\hat{\mathbf{E}} = \frac{1}{2} \left(\hat{\mathbf{A}}^{\mathsf{T}} \cdot \hat{\mathbf{A}} - (\mathbf{I} - \mathbf{N} \mathbf{N}) \right), \tag{2}$$

where N and n are the reference and deformed surface normal vectors, and X and x(X,t) are associated with the vessel surface. The left Cauchy-Green surface deformation tensor, $\hat{\mathbf{A}}^T \cdot \hat{\mathbf{A}}$, has two non-zero eigenvalues, λ_1^2 and λ_2^2 , where λ_1 and λ_2 are the stretch ratios along the principal axes on the surface. The corresponding principal strain components are $\frac{\lambda_1^2 - 1}{2}$, i = 1, 2. In this 2D form, the three-dimensional Cauchy stress tensor, σ , is replaced by surface traction tensor, τ , as $\tau = \sigma h$, which is expressed as

$$\tau = \frac{1}{J_S} \hat{\mathbf{A}} \cdot \frac{\partial W_S}{\partial \hat{\mathbf{F}}} \cdot \hat{\mathbf{A}}^T, \tag{3}$$

where $J_S = \lambda_1 \lambda_2$ is the surface area dilation, and W_S is the surface strain energy defined per unit area in the reference configuration, which relates to the volume strain energy function W as $W_S = Wh$ [54–56]. Likewise, the 2D (surface) Young's modulus E_S is related to the 3D modulus E_S by $E_S = Eh$. The principal traction components τ_1 and τ_2 can further be written as

$$\tau_1 = \frac{1}{\lambda_2} \frac{\partial W_S}{\partial \lambda_1}, \qquad \tau_2 = \frac{1}{\lambda_1} \frac{\partial W_S}{\partial \lambda_2}. \tag{4}$$

Due to material isotropy, the traction tensor can be expressed using the above components as

$$\tau = \tau_1 \ e_1 \otimes e_1 + \tau_2 \ e_2 \otimes e_2 \tag{5}$$

where e_1 and e_2 are the unit eigenvectors of $\hat{\mathbf{A}}^T \cdot \hat{\mathbf{A}}$.

Several hyperelastic material models have been considered in the current study. The 2D strain energy functions for these models may be uniformly and conveniently expressed in terms of a surface shear modulus G_S as follows:

Mooney-Rivlin model:
$$W_S^{MR} = \frac{G_S}{2} \left[\Psi \left(I_1 + 2 + \frac{1}{I_2 + 1} \right) + (1 - \Psi) \left(\frac{I_1 + 2}{I_2 + 1} + I_2 + 1 \right) \right], \tag{6}$$

Neo-Hookean model:
$$W_S^{NH} = \frac{G_S}{2} \left(I_1 + 2 + \frac{1}{I_2 + 1} \right), \tag{7}$$

Strain hardening model of Skalak et al. [57]
$$W_S^{Sk} = \frac{G_S}{4} \left(I_1^2 + 2I_1 - 2I_2 + CI_2^2 \right). \tag{8}$$

Additionally, the simplest case of linear elasticity is also implemented using 2D Hooke's Law as mentioned later. Here we use "Hooke's Law" to mean the constitutive model of a linear elastic material, following Fung in §2.6 of [1]. In the above, $I_1 = 2tr\left\{\hat{\mathbf{E}}\right\} = \lambda_1^2 + \lambda_2^2 - 2$, and $I_2 = J_S^2 - 1$ are invariants of $\hat{\mathbf{E}}$, and Ψ is a material parameter ranging between 0 and 1 which controls the contribution of normal stretch. The shear modulus G_S is related to the surface Young's modulus as

$$G_S = \frac{E_S}{2\left(1 + \nu_s\right)},\tag{9}$$

where v_s is the surface Poisson ratio. The Neo-Hookean material is a special case of the Mooney-Rivlin model where Ψ is at its maximum value of 1. Both the Mooney-Rivlin and Neo-Hookean models represent rubber-like materials that are strain softening, and they do not offer any resistance against area dilation. In contrast, Skalak's model is strain hardening, and it offers explicit resistance to area dilation with the associated modulus CG_S [56,57]. Note that the invariant I_2 is a measure of area dilation.

The principal elastic tensions for the above models are given below for τ_1 . The other component can be found by interchanging the indices.

Mooney-Rivlin:
$$\tau_1 = \frac{G_S}{\lambda_1 \lambda_2} \left(\lambda_1^2 - \frac{1}{\left(\lambda_1 \lambda_2\right)^2} \right) \left[\Psi + \lambda_2^2 (1 - \Psi) \right], \tag{10}$$

Neo-Hookean:
$$\tau_1 = \frac{G_S}{\lambda_1 \lambda_2} \left(\lambda_1^2 - \frac{1}{\left(\lambda_1 \lambda_2\right)^2} \right), \tag{11}$$

Skalak et al:
$$\tau_{1} = \frac{G_{S}}{\lambda_{1}\lambda_{2}} \left\{ \lambda_{1}^{2} \left(\lambda_{1}^{2} - 1\right) + C\left(\lambda_{1}\lambda_{2}\right)^{2} \left[\left(\lambda_{1}\lambda_{2}\right)^{2} - 1\right] \right\},\tag{12}$$

Hooke's Law [56]:
$$\tau_1 = \frac{G_S}{1 - v_s} \left[\lambda_1^2 - 1 + v_s \left(\lambda_2^2 - 1 \right) \right]. \tag{13}$$

For a meaningful comparison, the different models must converge in the limit of small deformation, and the material parameters must be related to satisfy this consistency. The Mooney-Rivlin and Neo-Hookean models are volume incompressible, hence at small deformation they approach the incompressible Hooke's law for $v_s = 0.5$. The surface shear modulus for each is, likewise, identical at small deformation. Skalak's model also has an equivalent shear modulus, and the constant C is related to v_s as $v_s = \frac{C}{1+C}$ [56]. Taking C = 1 makes it incompressible and thus comparable to the other models.

2.3. Finite element method for wall mechanics

A finite element method is used to solve elastic tensions [58]. The surface of the vessel is discretized using triangular elements, the vertices (nodes) of which make up a Lagrangian framework (Fig. 1(b)). We assume that the elements remain flat upon deformation. The deformed elements are transformed to the plane of undeformed elements using rigid-body rotation and translation. The problem then reduces to a 2D planar deformation. For each element, a local 2D coordinate system lying in the element plane is introduced. The displacement field in each element is assumed to vary linearly and in the local coordinate it is expressed as $\hat{v} = \sum H_i \hat{v}_i$, where

i = 1, 2, 3 denote the three vertices of the element, and \hat{v}_i and H_i are, respectively, the local displacement and shape function of vertex i. Then, \hat{A} , λ_1 , λ_2 , and τ for each element are computed. Note that

$$\lambda_i^2 = \frac{1}{2} \left[G_{11} + G_{22} \pm \sqrt{\left\{ \left(G_{11} - G_{22} \right)^2 + 4G_{12}^2 \right\}} \right], \qquad i = 1, 2,$$
(14)

where $\mathbf{G} = \hat{\mathbf{A}}^T \cdot \hat{\mathbf{A}}$.

For the fluid/structure coupling discussed later, it is useful to obtain the elastic surface force density (force per unit area) f_e at each Lagrangian vertex. For this, the in-plane (2D) force f_i^{Δ} at the vertex i in the local (element-attached) coordinate is first obtained. This may be obtained from τ as

$$\boldsymbol{f}_{i}^{\Delta} = \frac{\partial H_{i}}{\partial \hat{\boldsymbol{V}}} \cdot \mathbf{P},\tag{15}$$

where $\mathbf{P} = \lambda_1 \lambda_2 \mathbf{\tau} \cdot \hat{\mathbf{A}}^{-T}$ is the first Piola-Kirchhoff stress tensor and $\hat{\mathbf{V}}$ represents the local coordinate attached to and in the plane of the undeformed element. Alternatively, this can be obtained from the strain energy function using the principle of virtual work as

$$\boldsymbol{f}_{i}^{\Delta} = \frac{\partial W_{S}}{\partial \hat{\boldsymbol{v}}_{i}} = \left(\frac{\partial W_{S}}{\partial \lambda_{1}}\right) \left(\frac{\partial \lambda_{1}}{\partial \hat{\boldsymbol{v}}_{i}}\right) + \left(\frac{\partial W_{S}}{\partial \lambda_{2}}\right) \left(\frac{\partial \lambda_{2}}{\partial \hat{\boldsymbol{v}}_{i}}\right). \tag{16}$$

The local force is then transferred to the global coordinate using the transformation matrix $\mathbf{R} = e^0 e^d$ as $\mathbf{f}_i = \mathbf{R}^T \mathbf{f}_i^\Delta$ where e^d and e^0 are unit vectors attached to the deformed element and the global coordinate, respectively. Since each vertex shares six triangular elements, the resultant elastic force density \mathbf{f}_e at any vertex is obtained by vector resultant of the forces \mathbf{f}_m contributed by all the surrounding elements which share that vertex:

$$f_e = \sum_{m \in M} f_m,\tag{17}$$

where M represents the number of elements surrounding the vertex, and the summation is over $m \in M$.

2.4. Modeling bending

When the external pressure is greater than the internal pressure, the vessel may collapse, like the buckling of a thin-walled structure [1]. In such cases, forces arising from bending become significant. To model the bending resistance, an energy-based approach is employed. The bending energy of a 2D flat plate was generalized by Canham and Helfrich to model highly deformable thin-walled surfaces with significant variations in curvature as [59]

$$W_b = \frac{E_b}{2} \int_{S} (2\kappa - c_0)^2 dS,$$
 (18)

where E_b is a bending modulus, κ is the mean curvature, and c_0 is a "spontaneous" curvature. In the linear elastic limit, the bending modulus is related to the Young's modulus by $E_b = \frac{Eh^3}{12(1-\nu^2)}$. It was shown in Pozrikidis [54] that the spontaneous curvature c_0 represents twice the mean curvature of the undeformed configuration. Additionally, they showed that this form of bending energy, when reduced to 2D, is consistent with the generic linear constitutive model of bending moments with respect to curvature, suggesting the model is suited for general applications. A bending force density (per unit area of the surface) can be obtained by taking the Fréchet derivative of eq. (18) as [60]

$$\boldsymbol{f}_b = E_b \left[(2\kappa + c_0) \left(2\kappa^2 - 2\kappa_g - c_0 \kappa \right) + 2\Delta_{LB} \kappa \right] \boldsymbol{n}, \tag{19}$$

where κ_{g} is the Gaussian curvature, and Δ_{LB} is the Laplace-Beltrami operator.

Now we discuss the numerical computation of the bending force density. For this, first the mean and Gaussian curvatures at vertex of the triangulated vessel surface are obtained by fitting a locally quadratic surface [61]. The curvatures κ and κ_g can be explicitly expressed in terms of the coefficients of the fitted surface. Several approximations are possible to obtain the Laplace-Beltrami operator on a triangulated surface [62]. The specific one used here is given as

$$\Delta_{LB}\kappa_i = \frac{1}{2S} \sum_{j \in N} \mathbf{n}_j \cdot \nabla_s k_j + \nabla_s k_{j+} \left\| \mathbf{x}_j - \mathbf{x}_{j+} \right\|,\tag{20}$$

or any vertex i located at x_i , where the summation is over N number of vertices that are the immediate neighbors (first ring) of the vertex i, and the index j represents each of these neighboring vertices. The vertices of a triangle that share the vertex i are i, j, j+, and n_j is the unit vector that is normal to the edge defined by j, j+. Also, S is the sum of the areas of all surrounding M triangles with the common vertex i, and ∇_s is the surface gradient at any vertex. Before obtaining $\nabla_s k_j$, we first compute the surface gradient of κ in each surrounding element m assuming κ varies linearly within each element:

$$\nabla_{m}\kappa = \frac{1}{4S_{m}^{2}} \left\{ \kappa_{i} \left[\left(\mathbf{x}_{i} - \mathbf{x}_{j} \right) \cdot \left(\mathbf{x}_{j} - \mathbf{x}_{j+} \right) \left(\mathbf{x}_{j+1} - \mathbf{x}_{i} \right) + \left(\mathbf{x}_{i} - \mathbf{x}_{j+} \right) \cdot \left(\mathbf{x}_{j+} - \mathbf{x}_{j} \right) \left(\mathbf{x}_{j} - \mathbf{x}_{i} \right) \right]$$

$$(21)$$

+ similar terms with i and j interchanged and i and j + interchanged },

where S_m is the area of element m. Then, $\nabla_s k_i$ is computed as the weighted average as

$$\nabla_{s} k_{j} = \frac{1}{S} \sum_{m \in M} S_{m} \nabla_{m} \kappa. \tag{22}$$

It was shown by Peskin that the elastic force density of a material under an arbitrary deformation can be found by taking the Fréchet derivative of its elastic potential energy [25]. For an elastic body immersed in fluid, by using the principle of stationary action it is shown that this force density acts as a coupling term between the body and surrounding fluid. In the case of a vanishingly thin membrane, the elastic body becomes a 2D surface that sustains an elastic surface force density, which becomes singular in the Eulerian description of the 3D domain. For this 2D membrane, Peskin explicitly wrote the total elastic potential as the sum of the energetic contributions of both the in-plane deformation and curvature, classically known as the strain energy and bending energy, respectively. By taking the derivative, he then expressed the total elastic force density as the sum of both the in-plane elastic and bending force densities [63]. Motivated by this, the net force in the vessel surface is written as the sum of the elastic force and the force due to bending,

$$f = f_e + f_h. ag{23}$$

Note that this approach of adding force densities has been successfully used in other problems with thin elastic membranes [55,56,63–66].

2.5. Flow dynamics and fluid/structure coupling

As is the case in immersed boundary methods, the entire computation domain, including the interior and exterior of the vessel, contains fluid. The fluid is assumed to be incompressible, and the fluid motion is governed by the continuity and Navier-Stokes equations as

$$\nabla \cdot \boldsymbol{u} = 0$$
, and $\rho \frac{D\boldsymbol{u}}{Dt} = -\nabla P + \mu \nabla^2 \boldsymbol{u}$ (24)

These equations are solved in the entire computation domain (Fig. 1(a)) which is discretized using an Eulerian rectangular mesh of uniform size.

The immersed boundary method used for the fluid/structure coupling is now discussed. As discussed in § 1, there are two choices available for the coupling of complex deforming or non-deforming boundaries to the surrounding fluid. One is the continuous forcing method, where the resultant force from deformation (i.e., eq. (23)) is introduced as a coupling force to the Navier-Stokes equations

$$\rho \frac{D\mathbf{u}}{Dt} = -\nabla P + \mu \nabla^2 \mathbf{u} + \mathbf{F} \tag{25}$$

where

$$F(\mathbf{x},t) = \int_{S} f(\mathbf{x}',t) \,\delta(\mathbf{x} - \mathbf{x}') \,dS,\tag{26}$$

and x' is any location on the surface $S \in \mathbb{R}^3$, $x \in \mathbb{R}^3$ is the Eulerian variable, and δ is the 3D Dirac delta function [25]. Due to the delta function, F is infinite at x = x' and zero elsewhere representing the zero-thickness vessel wall. To avoid the singularity of δ in the numerical implementation, a discrete form with a finite spread in \mathbb{R}^3 is used, effectively treating the infinitely thin interface as a diffuse surface. Different discrete representations of δ are available in the literature, and here we use the following form [25]

$$\delta\left(\mathbf{x} - \mathbf{x}'\right) \approx D\left(\mathbf{x} - \mathbf{x}'\right) = \begin{cases} \frac{1}{(2\hbar)^3} \prod_{i=1}^3 \left[1 + \cos\left\{\frac{\pi}{\hbar} \left(x_i - x_i'\right)\right\}\right] & \text{if } |x_i - x_i'| \le \hbar, \\ 0 & \text{else,} \end{cases}$$
(27)

and,

$$F\left(x_{m}\right) = \sum_{n} f\left(x_{n}'\right) D\left(x_{m} - x_{n}'\right) \Delta S_{n},\tag{28}$$

where $\hbar = 2\Delta_E$ (where Δ_E is the size of the unit Eulerian cell), ΔS_n is the interface area associated with each vertex, m and n indicate Eulerian and Lagrangian points, respectively, and the summation is over the Lagrangian points. The force coupling approach has been commonly used for liquid-liquid or liquid-air interfaces governed by surface tension, and biological cell membranes governed by more complex material behavior [26,31–37]. Once the fluid velocity is obtained at any time t by solving eq. (25), the interface (i.e., the vessel wall in the present case) is advected using the local fluid velocity as

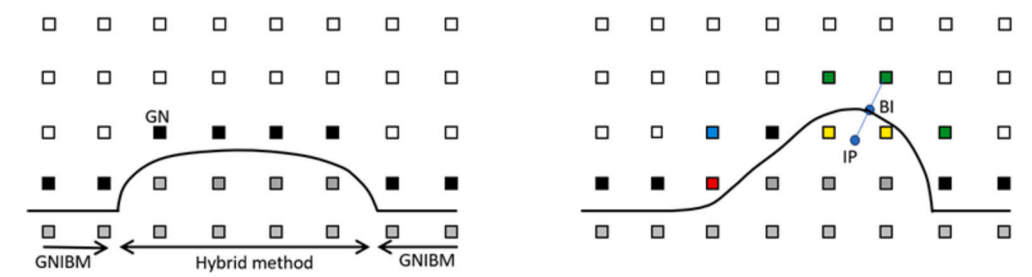


Fig. 2. Eulerian node classification for the deforming interface. GN: ghost node, IP: image point, BI: boundary intercept. Black and gray squares are GNs and fluid nodes, respectively. Red; a fluid node that becomes a GN; blue; a GN declassified; green; exterior nodes that are newly classified as GN; vellow; previous GNs that become fluid nodes. (For interpretation of the colors in the figure(s), the reader is referred to the web version of this article.)

$$\frac{d\mathbf{x}'}{dt} = \mathbf{u}_w \left(\mathbf{x}', t \right),\tag{29}$$

where u_w is the interface velocity that is obtained as the weighted average of the surrounding fluid velocity using the delta function as

$$\mathbf{u}_{w}\left(\mathbf{x}',t\right) = \int_{\mathbf{x}} \mathbf{u}\left(\mathbf{x},t\right)\delta\left(\mathbf{x}-\mathbf{x}'\right)d\mathbf{x}.\tag{30}$$

The second potential choice for the fluid/structure coupling is a direct forcing method, such as the ghost-node immersed boundary method (GNIBM) which has been used for complex rigid interfaces, moving rigid bodies, and deforming bodies [46]. The general idea of the GNIBM is that a velocity constraint is enforced at certain Eulerian points which satisfies the no-slip condition at the interface by interpolation. The interface can be defined analytically, or, in the case of a complex geometry, using a surface mesh which differentiates the region of interest (which, in this case, is the interior of the vessel) from the rest of the domain. The velocity constraints are imposed at the Eulerian nodes immediately neighboring the vessel exterior, termed the ghost nodes (GN). The point which mirrors a GN over the vessel wall is its image point (IP), and the line joining the GN and IP (the normal probe) orthogonally intersects the wall at the boundary intercept (BI) (Fig. 2). The imposed velocity u_{GN} is chosen so the no-slip condition $u(x') = u_{w}$ is satisfied at the BI; hence, $u_{BI} = u_w$. One can approximate u_{BI} to second-order accuracy as the average of the velocities at the GN and IP [46]. Then, the constraint to be implemented at the GN becomes

$$\boldsymbol{u}_{GN} = 2\boldsymbol{u}_{BI} - \boldsymbol{u}_{IP}. \tag{31}$$

In general, the IPs do not coincide with the Eulerian nodes. A standard trilinear interpolant is used to obtain the velocity at an IP from the surrounding Eulerian nodes as [46]

$$u_{IP} = \sum_{l=1}^{8} \beta_l u_l \tag{32}$$

where each *l* represents a Eulerian mesh point surrounding the IP, and β_l is the weight of node *l* based on the distance from the IP. For the present problem, a continuous force coupling method leads to excessive axial stretch of the vessel at the upstream pinned end, and a nonphysical crumpling at the downstream end. Note that the thin-walled tube considered here cannot sustain compressive stress, which leads to the crumpling. One could mitigate this problem by imposing a restoring force which counters the axial motion; however, our numerical experiments showed that this approach leads to numerical instability. Further, when this method is applied to a rigid tube, the volume flow rate was significantly reduced compared to analytical solutions. Another possibility is to use a full GNIBM implementation in which the wall is represented using point masses that are moved following Newton's law. In this case, the net force would be the sum of the membrane force (f) and the transmural pressure (i.e., difference between the internal and external pressure) at any location across the vessel wall. We find that this approach led to a stable and physically realistic vessel deformation, but with a large amount of fluid leakage.

To avoid such issues, we developed a hybrid of the sharp and diffuse interface methodologies. The approach seeks to resolve the fluid-structure interaction using the two different methods in each cartesian direction. No axial wall motion is allowed, and the zero-velocity (no-slip) condition in the axial (x) direction is enforced using the GNIBM. For the two normal directions (y and z), the wall is allowed to advect with the surrounding fluid, and the continuous forcing method couples the structural mechanics to the fluid.

This hybrid method can be represented using a compact form as follows. The fluid/structure coupling in general involves three terms: the body force F, the BI velocity u_{BI} , and the interface velocity u_w . The forms of these terms vary based on the methodology, and they can be used to define the hybridization. In the limit of a full sharp-interface or a full continuous forcing method, the coupling terms become

Sharp-Interface:
$$F = \mathbf{0}$$
, $\mathbf{u}_{GN} = 2\mathbf{u}_{BI} - \sum_{m=1}^{8} \beta_m \mathbf{u}_m$, $\mathbf{u}_w = \mathbf{0}$, (33)

Sharp-Interface:
$$F = \mathbf{0}$$
, $\mathbf{u}_{GN} = 2\mathbf{u}_{BI} - \sum_{m=1}^{8} \beta_m \mathbf{u}_m$, $\mathbf{u}_w = \mathbf{0}$, (33)

Continuous Forcing: $F = \int_{S} f \delta \left(\mathbf{x} - \mathbf{x}' \right) d\mathbf{x}'$, $\mathbf{u}_{GN} = \mathbf{u}$, $\mathbf{u}_w = \int_{S} \mathbf{u} \delta \left(\mathbf{x} - \mathbf{x}' \right) d\mathbf{x}$. (34)

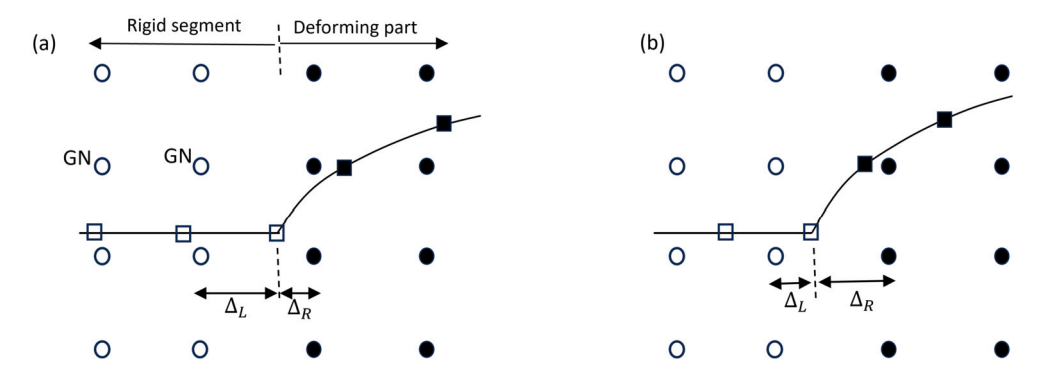


Fig. 3. Placement of the rigid-to-deforming parts transition location. Circles indicate Eulerian mesh points; filled circles are the points to which wall forces are spread. Squares indicate Lagrangian points on the vessel surface: filled ones are the moving points from which the forces are spread. (a) $\Delta_L > \Delta_R$: weaker influence of the GN and hybrid conditions at the transition point. (b) $\Delta_L < \Delta_R$: stronger influence of the GN constraint.

In eq. (34), $u_{GN} = u$ indicates that no velocities are prescribed at the GNs. Then, the hybrid approach can be expressed as

$$Hybrid: \mathbf{F} = \begin{bmatrix} 0 \\ \int_{S} f_{y}\delta(\mathbf{x} - \mathbf{x}') d\mathbf{x}' \\ \int_{S} f_{z}\delta(\mathbf{x} - \mathbf{x}') d\mathbf{x}' \end{bmatrix}, \mathbf{u}_{GN} = \begin{bmatrix} -\sum_{l=1}^{8} \beta_{l}u_{l} \\ v \\ w \end{bmatrix}, \mathbf{u}_{w} = \begin{bmatrix} 0 \\ \int_{\mathbf{x}} v\delta(\mathbf{x} - \mathbf{x}') d\mathbf{x} \\ \int_{\mathbf{x}} w\delta(\mathbf{x} - \mathbf{x}') d\mathbf{x} \end{bmatrix}, (35)$$

where $f = \begin{bmatrix} f_x \\ f_y \\ f_z \end{bmatrix}$ and $\mathbf{u} = \begin{bmatrix} u \\ w \end{bmatrix}$. The wall is advected using the v and w components of the fluid velocity, and only the y and z force components are applied to the fluid. The vessel wall force is spread to both the internal and external fluid, and, likewise, the wall velocity is interpolated from both. Once the flow field is solved for a time t, the wall is advected in the y and z directions following eq. (29) using the second-order Runge-Kutta method.

The hybrid method is used for the deforming section of the tube, whereas the full GNIBM is used for the rigid sections at the upstream and downstream ends (Fig. 2).

Careful consideration is required at the transition between the rigid and deforming segments, where the GNIBM and hybrid methods interface. Overlapping the influence of two methods risks over-constraining the problem, leading to inaccuracy and numerical instability. The transition point is defined as the *x*-location of the last Lagrangian nodes of the rigid segment. The force at the transition node must not be spread to the fluid, as the fixed nodes cause unphysically large elastic forces to generate. The force is only spread to all relevant nodes in the deforming region. Interpolation of the membrane velocity occurs over the same stencil as the force spreading for consistency. This creates a strict demarcation of methodologies on either side of the transition point.

Placement of the transition point relative to the Eulerian grid also impacts the flow to an extent (Fig. 3). The interpolation techniques differ between methods: standard trilinear for the GNIBM, and delta function weighted averaging for the continuous forcing method. These reflect the sharp versus diffuse natures of the methods, where the former acts on points within a single grid space, and the latter acts over two grid spaces. If the transition point is placed close to the last Eulerian point inside the rigid segment, the GN constraint has too strong of an influence, and the flow does not have time to properly adjust to the force from the deforming segment. Additionally, the first deforming elements would have a diminished force contribution, as many nearby Eulerian nodes are in the rigid segment, where no force can be spread. These issues can cause spurious oscillations in the pressure at the transition. This situation may be avoided by placing the transition point close to the first Eulerian node in the *deformable* segment. The impact of the GN constraint at the transition point is then weakened, allowing the flow to adjust within the rigid segment.

2.6. GN and BI update for the deforming interface

As the vessel wall deforms, some Eulerian mesh points outside of the vessel may enter the vessel interior, and vice versa (Fig. 2). As a result, GNs, BIs, IPs, and interpolation matrices must be updated at every step of the time marching. This process is generally time consuming for an arbitrary deformation. As such, a fast and parallelizable algorithm was developed which relies on finding the ghost node-"intercept element" pairs following a procedurally determined pathway. Note that such updates are needed only for the *u*-component of the fluid velocity since it is treated using the GNIBM. The update follows three steps as discussed below.

(i) Finding the intercept element for each GN

For any timestep, we start with the GNs from the previous timestep and find their intercept elements (IE). The IE of a GN is defined as the triangular element on the vessel surface mesh that contains the BI. To find the updated IE, an efficient algorithm has been developed which minimizes computation. For this, the "projected volume" (PV) of an element is introduced as the imaginary triangular prism generated by projecting the element face along its normal. The normal probe of a nearby GN lying inside an

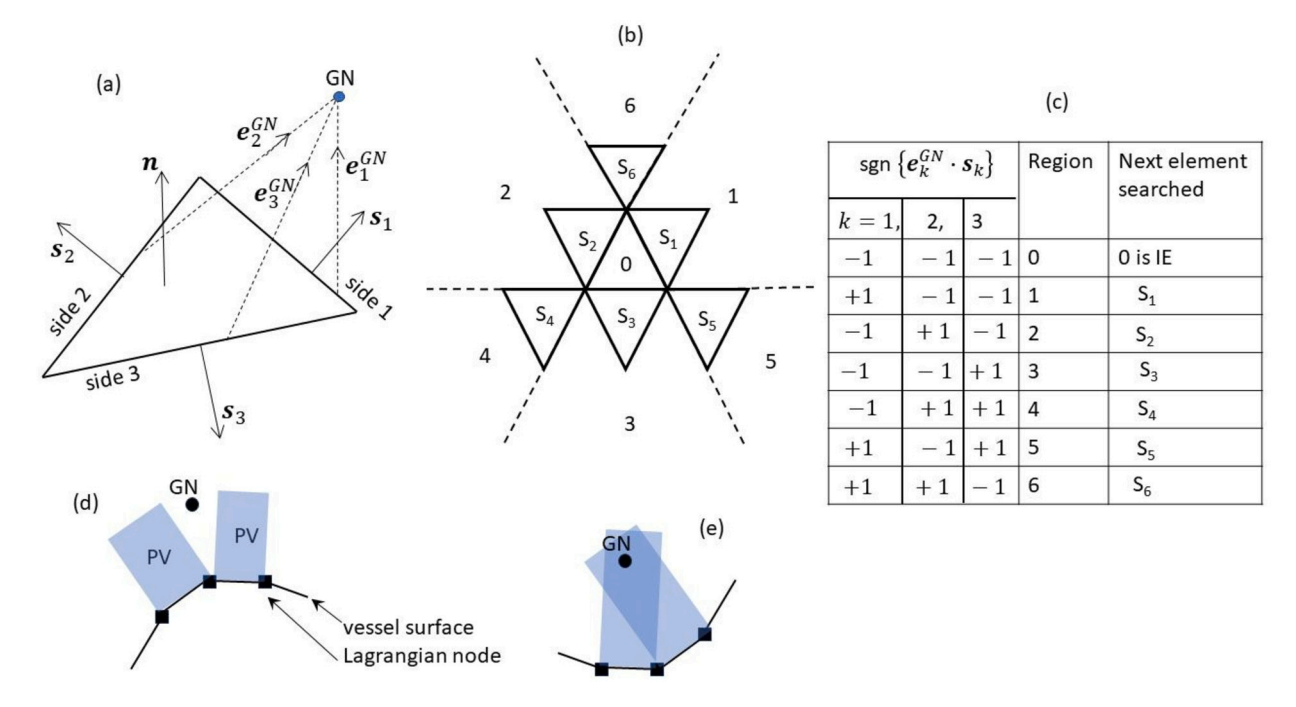


Fig. 4. Procedure for finding GN-IE pair. (a): a surface element and a nearby GN showing vectors s_k and e_k^{GN} . (b) Path to search the IE. 1–6 indicates different regions based on the sign of $s_k \cdot e_k^{GN}$ and $S_1 - S_6$ are the elements searched. (c) Table shows the regions and element searched for combination of \pm signs. 0 indicates that the element is the IE. (d), (e) situations when a GN may not lie within a projected volume (PV) and when a GN can lie within multiple PVs.

element's PV must intersect the element; therefore, the IE of a particular GN is the element whose PV contains the GN. The process begins by checking if a GN falls within the PV of a convenient nearby element, which is generally the IE found at the previous time step. To describe the element's projected geometry, the vector s_k (k = 1, 2, 3) is introduced which lies in the plane of the element and is an outward normal to side k. We also introduce e_k^{GN} as the vector from side k to the GN (Fig. 4(a)), such that the scalar product $s_k \cdot e_k^{GN}$ describes the GN's position relative to side k. The vectors' origins are arbitrary, so long as they are at some point on side k. With this, we see that the PV contains the GN if all three $s_k \cdot e_k^{GN}$ are negative, determining that the current element is the IE.

If all three products $s_k \cdot e_k^{GN}$ are not negative, the PV does not contain the GN, and the next most likely neighboring element is checked. An algorithm has been developed in which the surrounding elements are searched along a path that ensures an IE is found. This is done by checking the signs of the three products $s_k \cdot e_k^{GN}$. The specific combination of \pm signs indicates the region other than PV that the GN lies in, as illustrated in Fig. 4. There are six such regions, as indicated by 1–6 in the figure, and the next element checked for a possible GN-IE pair is based on the signs of $s_k \cdot e_k^{GN}$ as given in Fig. 4(b), (c).

Occasionally, a GN may not lie within the PV of any surface element. This indicates that the corresponding BI falls between neighboring elements. This happens, for example, for an inflated vessel (Fig. 4(d)). These cases can be uniquely determined using the history of the search and the knowledge of element connectivity. For example, if a search repeats between two elements, then the BI must lie on their common edge. For three repeated elements, the BI is located on the common vertex.

Alternatively, a single GN may lie within multiple PVs, e.g., in the case of a collapsing vessel (Fig. 4(e)). This results in multiple possible BIs for the same GN. In such cases, any choice of IE is valid, and the GN can be regarded as having multiple BIs. As the BI velocity is enforced by interpolation, this GN constrains each BI velocity to second-order accuracy. A sufficiently fine computational mesh will ensure that any choice of IE (and its corresponding BI) results in the same prescribed GN velocity, otherwise the wall boundary conditions cannot be correctly imposed. Therefore, it is sufficient to accept the first IE found during the search and its corresponding BI.

(ii) Checking for GN declassification and new GN identification

The updated IE is then used to check whether the old GN remains a GN in the current time step (Fig. 2). Further, this information is used to identify any new GNs, such that all GNs for the current time step are properly identified by the end of the declassification. This relies on the slow motion of the wall (no more than one Eulerian grid spacing per time step) ensuring that any new GNs must neighbor old GNs. First, we check if the old GN remains exterior; that is, $\mathbf{n} \cdot \mathbf{e}_k^{GN} > 0$, where \mathbf{n} is the outward normal of the IE. In this case, any neighboring fluid nodes which have exited the vessel become new GNs. If all neighboring fluid nodes have exited the vessel, this old GN is declassified. Otherwise, it remains a GN.

If $n \cdot e_k^{GN} < 0$, the node falls inside the vessel and is no longer a GN. Any neighboring nodes in the exterior now become GNs if they were not GNs in the previous step.

Step (i) is then repeated for these new GNs.

(iii) Calculation of new BIs, IPs, and interpolation matrices

Once the GN-IE pairs are found, the new BI calculation is straightforward as noted in § 2.5. The recomputing of IPs and interpolation matrix weighting coefficients β_m follows the same procedure outlined there.

The above method is parallelizable by sweeping over the GNs. However, to avoid any ambiguity, another sweep is performed over the exterior declassified GNs to ensure they do not have an interior neighbor. Furthermore, the IE search method developed does not require significant computation. Determining the PVs requires only 3 scalar products per element. The time step required for stable fluid and wall mechanics ensures that the interface moves no more than one Eulerian grid spacing per time step. As such, the majority of GNs remain unchanged from one time step to the next. In these cases, it is sufficient to search a maximum of three elements to locate the IE. Many cases will require fewer, as those GNs with unchanging IEs require only one element to be searched. The most expensive searches are those for new GNs, where a neighboring node's IE is taken as the starting element, which may not neighbor the IE. However, such cases occur the least often which helps to offset their cost.

2.7. Flow solver

The flow solver is based on a projection-based method for incompressible flows, along with coupled finite-volume/spectral methods for spatial discretization. A staggered-grid implementation is considered for the fluid velocity components, which are defined at the computational cell faces, and the pressure, defined at the cell center. As noted in our prior work [35], the use of the staggered grid naturally retains the strong coupling between the velocity and pressure without any special treatment, reducing the spurious pressure oscillations often associated with moving boundaries. Moreover, it allows an explicit implementation of the GN constraints as discussed later. As noted before, the governing equation is the full Navier-Stokes equations including the force coupling terms. A four-step projection method advances the velocity and pressure fields from time step n to n+1 [67]. An advection-diffusion equation is first solved which yields an intermediate velocity \hat{u} , followed by u^* , which is not divergence-free. Next steps involve solving a Poisson equation for pressure and correcting u^* to make it divergence-free. The diffusion terms are treated using the semi-implicit Crank-Nicolson scheme, and the nonlinear and force coupling terms are treated explicitly using the second-order Adams-Bashforth scheme.

Advection-diffusion:
$$\rho \frac{\hat{\boldsymbol{u}} - \boldsymbol{u}^n}{\Delta t} = -\nabla P^n + \frac{\mu}{2} \left[\nabla^2 \hat{\boldsymbol{u}} + \nabla^2 \boldsymbol{u}^n \right] - \left[\frac{3}{2} \boldsymbol{N}^n - \frac{1}{2} \boldsymbol{N}^{n-1} \right], \tag{36}$$

where $N = \rho u \cdot \nabla u - F$

Intermediate velocity:
$$\rho \frac{u^* - \hat{u}}{\Delta t} = \nabla P^n, \tag{37}$$

Poisson equation:
$$\nabla^2 P^{n+1} = \rho \frac{\nabla \cdot \mathbf{u}^*}{\Delta t}, \tag{38}$$

Pressure correction:
$$\rho \frac{\mathbf{u}^{n+1} - \mathbf{u}^*}{\Delta t} = -\nabla P^{n+1}. \tag{39}$$

It may be noted that, alternatively to the four-step method, one could use a three-step method where the advection-diffusion equation does not include the $-\nabla P^n$ term, thereby directly yielding u^* . Our numerical experiments, however, showed that the pressure field is not well-behaved with the three-step scheme at a high transmural pressure. Specifically, the 3-step method leads to nonphysical pressure oscillations near the computation domain boundary around the vessel inlet where the transmural pressure difference is maximal. In contrast, the 4-step method resolves the pressure change to the grid order.

The spatial derivatives in the advection-diffusion equation are treated using second-order discretization. This equation is solved using an Alternating Direction Implicit (ADI) scheme so that the matrices at each ADI step can be inverted using the fast tridiagonal matrix inversion. The ADI scheme is implemented in four steps; the first step handles the explicit terms, while the remaining three steps handle the implicit sweeps in three directions.

$$\rho \frac{\hat{\boldsymbol{u}}^{***} - \boldsymbol{u}^n}{\Delta t} = -\nabla P^n + \frac{\mu}{2} \nabla^2 \boldsymbol{u}^n - \left[\frac{3}{2} \boldsymbol{N}^n - \frac{1}{2} \boldsymbol{N}^{n-1} \right], \tag{40}$$

$$\rho \frac{\hat{\boldsymbol{u}}^{**} - \hat{\boldsymbol{u}}^{***}}{\Delta t} = \frac{\mu}{2} \frac{\partial^2 \hat{\boldsymbol{u}}^{**}}{\partial x^2},\tag{41}$$

$$\rho \frac{\hat{\mathbf{u}}^* - \hat{\mathbf{u}}^{**}}{\Delta t} = \frac{\mu}{2} \frac{\partial^2 \hat{\mathbf{u}}^*}{\partial y^2},\tag{42}$$

$$\rho \frac{\hat{\mathbf{u}} - \hat{\mathbf{u}}^*}{\Delta t} = \frac{\mu}{2} \frac{\partial^2 \hat{\mathbf{u}}}{\partial z^2}. \tag{43}$$

The Poisson equation must be solved implicitly to satisfy the divergence-free condition. We treat the z direction as periodic and use the Fourier expansion, thereby reducing the 3D Poisson equation to a 2D problem for each Fourier mode, which can be solved using a fast direct matrix inversion. Details can be found in Mittal and Balachander [68].

The GN constraint enforced to achieve the no-slip condition is implemented at the advection-diffusion step. As noted in [35], the implicit use of the constraint results in the loss of the tridiagonal nature of the matrices in the ADI scheme. Instead, we use an explicit form in which the velocity at time step n is used to obtain the IP values. Furthermore, the constraint is applied to the intermediate velocity $\hat{\boldsymbol{u}}$ as

$$\hat{u}_{GN} = 2u_{BI} - \sum_{l=1}^{8} \beta_l u_l^n, \tag{44}$$

where β are weighting coefficients for a trilinear interpolation of the image point velocity u_{IP} from the 8 surrounding nodes. It was shown by Choi and Moin that the intermediate velocity field is equal to the true velocity field up to second-order in time, i.e., $\hat{u} = u^{n+1} + \mathcal{O}(\Delta t^2)$ [67]. Therefore, applying the GN constraint at this step (eq. (36)) ensures that u^{n+1} obtained from eq. (39) at any GN is the prescribed velocity up to $\mathcal{O}(\Delta t^2)$. Further details can be found in [23,35,46].

2.8. Additional considerations

Since the Fourier transform is used for solving the Poisson equation for pressure, a boundary condition for pressure at the vessel surface, such as the zero normal derivative, is not applied. For very large transmural pressure, this can cause fluid leakage through a highly curved surface. A countering force proportional to the transmural pressure is applied to mitigate this effect. At each Lagrangian node, the internal and external pressures are interpolated from a normal probe that extends two Eulerian grid spaces from the surface. A force equal to the product of the pressure difference and the vertex area is applied normal to the surface in the direction of greater pressure. The force is spread only to nodes inside the vessel. Specifically, the same force spreading formulation is used (eq. (28)), but those nodes which fall outside the tube are ignored during computation.

Surface mesh smoothing is also needed for very large inflation and collapse. We use a mesh smoothing technique based on the idea of surface diffusion [69]. In this, a smoothing velocity is obtained as $u_s = -n\alpha\Delta_{LB}\kappa$, where α is a parameter that controls the degree of smoothing. The smoothing velocity is calculated every timestep and is added to the membrane velocity during the surface advection.

2.9. Dimensionless parameters

Solution of the governing equations and presentation of results are done in dimensionless form. For this, the undeformed vessel radius R_0 is taken as the length scale and the centerline velocity U_c of the Poiseuille flow in the undeformed vessel as the velocity scale. The pressure is scaled by ρU_c^2 , corresponding to a finite inertia condition. Dimensionless variables are indicated by a * when needed. The relevant dimensionless parameters are:

Reynolds number
$$Re = \frac{\rho U_c R_0}{\mu}$$

Dimensionless wall elasticity (or, deformability parameter) $\varepsilon = \frac{\mu U_c}{G_s}$

Dimensionless bending modulus $B = \frac{E_b}{R_o^2 G_s}$

In this scaling, the initial radius enters in the Reynolds number and bending modulus, but not in the deformability parameter. This choice is appropriate for finite inertia. Subsequently, relevant results are presented scaling by the initial radius. Generally, the parameters are held constant while the pressure difference between the inlet and outlet is altered which results in altering the vessel deformation and flow rate. To present such results in a convenient manner, we introduce the "baseline" pressure drop $\Delta P_0^* = P_0^* - P_L^*$ as the one that yields a dimensionless centerline velocity $U_c^* = 1$ for the undeformed vessel. Hence, $\Delta P_0^* = -\frac{4L^*}{Re}$ where L^* is the dimensionless total length of the vessel. A different applied pressure will be represented as $\frac{\Delta P}{\Delta P_0} = \frac{\Delta P^*}{\Delta P_0^*}$ which would yield values of U_c^* other than unity for any deviation from the baseline. Additional parameters specific to an inflating or collapsing vessel are defined later as needed. Also note that the wall to fluid mass density ratio is 1.

A convergence study of the mesh and domain size is presented in § 3.1.1.

3. Results

The validation of the method and its demonstration are presented now for inflating and deflating vessels at low and moderate fluid inertia.

3.1. Inflating vessel at weak inertia

In this section, the results for an inflating vessel at low fluid inertia corresponding to Re = 0.1 are presented. Initially, the fluid velocity is zero everywhere, and the vessel is undeformed with radius $R_0^* = 1$. The total length is $L^* = 4\pi$, which is subdivided into lengths $L_{inlet}^* = 1.18$ for the rigid inlet, $\check{L}^* = 11$ for the deforming segment, and $L_{outlet}^* = 0.39$ for the rigid outlet. At time $t^* = 0$, an inlet pressure $P_0^* > 0$ is applied, while the outlet and external pressures are held at zero as $P_L^* = P_{ext}^* = 0$. This setup is used for all inflation problems, unless stated otherwise. Also, no bending force is used for the inflation problem.

With the applied pressure difference, the flow develops, and the tube inflates until a steady deformed shape is attained, at which point the flow also reaches a steady state. Fig. 5(a) shows a 3D view of the inflated shape for an example simulation, and (b) shows

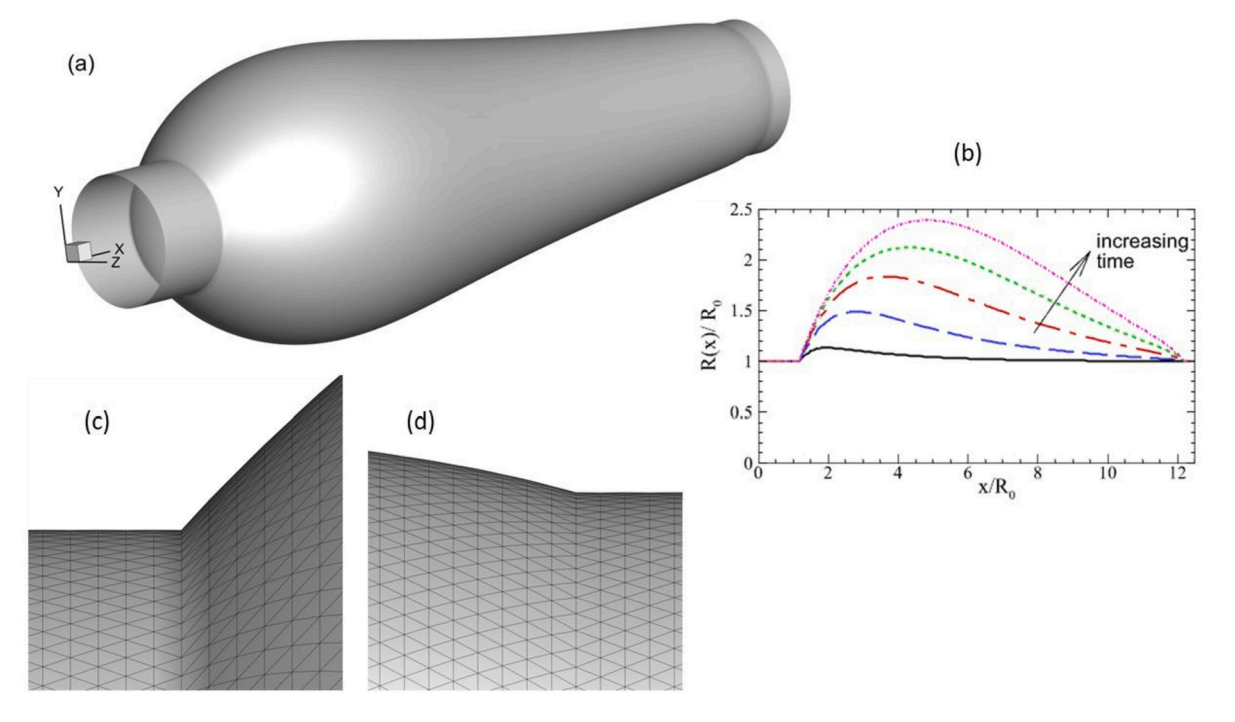


Fig. 5. Simulation of a vessel inflation. (a) 3D inflated shape, (b) time sequence of inflation, and (c) and (d) close-up of surface mesh around the up- and downstream transition regions.

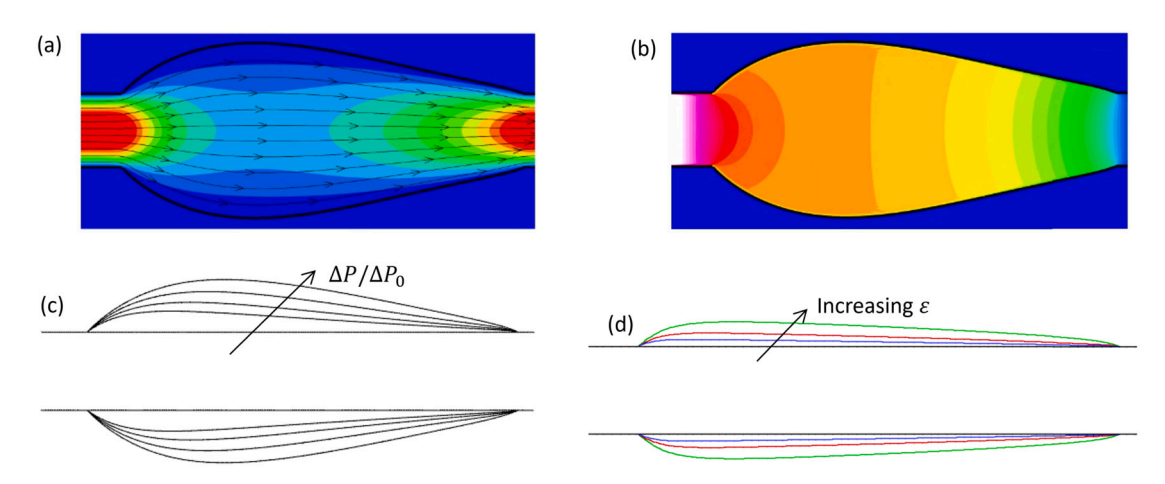


Fig. 6. (a) Streamwise velocity contours (1 to 10 at increment of 1; dimensionless) and streamlines. Parameters: Neo-Hookean (NH) model; $\frac{\Delta P}{\Delta P_0} = 4$; $\epsilon = 0.01$. (b) Pressure contours (0.1 increment) for the same case. (c) Steady deformed shapes under varying $\frac{\Delta P}{\Delta P_0} = 2.5, 3, 3.5, 4$ for the same NH model, $\epsilon = 0.01$. (d) Deformed shapes at varying $\epsilon = 0.005, 0.01, 0.02$ for Hookean model, $\epsilon = 0.05, \frac{\Delta P}{\Delta P_0} = 3$.

the time history of inflation. The radius of the deformed tube varies axially; it rapidly increases beyond the clamped entrance due to the high internal pressure. Downstream of the maximum radius, the deformation gradually decreases to the clamped exit. The change in the vessel radius is nearly 150% of the undeformed radius, indicating a high degree of deformation achievable by our model. Also note that the discontinuity of the slope of the vessel contours at the transition points between the rigid and deforming segments is well resolved by our method. Close-up views of the vessel surface mesh around these transition regions, which are most prone to mesh failure, are also shown. As seen, no mesh distortion is present even at such high deformation.

Further examples of generic behavior of an inflating vessel are considered in Fig. 6 where (a) and (b) show streamwise velocity contours, streamlines, and pressure contours at steady state. Axially varying velocity and pressure fields exist inside the vessel. Predicted pressure contours are normal to the deformed vessel wall, and the difference in internal and external pressure can be seen. Fig. 6(c) shows the deformed shapes for increasing pressure difference $\frac{\Delta P}{\Delta P_0}$. The influence of the deformability parameter ε is considered in Fig. 6(d) which shows increasing deformation as ε increases.

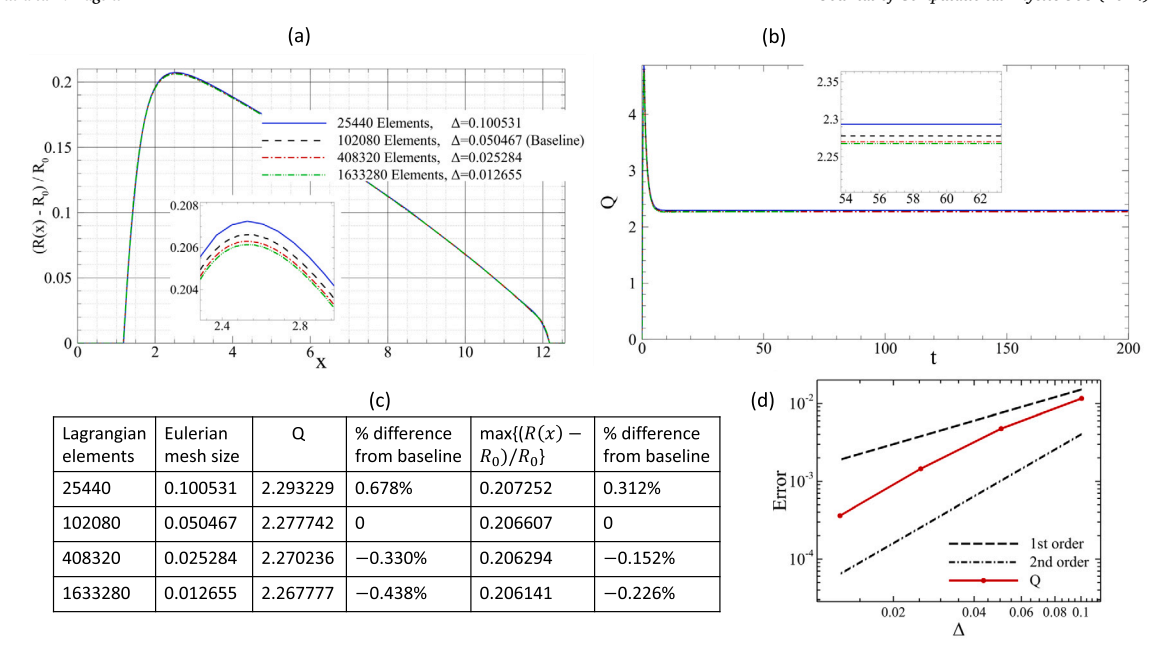


Fig. 7. Resolution test. (a) Circumferential strain defined as the relative radial displacement $(R(x) - R_0)/(R_0)$ along the centerline of an inflated vessel is shown for varying Lagrangian and Eulerian resolutions. "Elements" refers to the number of Lagrangian elements on the vessel surface, and Δ is the Eulerian mesh size relative to the undeformed vessel radius. (b) Flow rate versus time for the same cases as in (a). Insets show close-ups. (c) Numerical data are presented for different resolutions tested. "Baseline" refers to the resolution selected. (d) Convergence rate of the error in Q with Eulerian and Lagrangian grids varied in tandem. Parameters: Hookean model, v = 0.5, $\varepsilon = 0.02$; $\frac{\Delta P}{\Delta P} = 1$.

3.1.1. Resolution test

Grid convergence tests are shown in Fig. 7 in terms of the circumferential strain defined as the scaled radial displacement $(R(x) - R_0)/R_0$, and the flow rate through the vessel at steady state. Both the Eulerian grid discretizing the flow domain and the Lagrangian mesh discretizing the vessel surface are varied simultaneously to maintain the Eulerian/Lagrangian relative mesh sizes. Between the lowest and highest resolutions tested, the number of Eulerian mesh points in each direction varied by a factor of 8, and the number of wall surface elements varied by a factor of 8^2 . As seen, the finest resolution shows less than half a percent difference from the baseline, corresponding to an increase in the number of Eulerian points per direction and surface elements by 4 and 4^2 , respectively. As seen in Fig. 7(d), the method is nearly second-order following the second-order GN method with some error introduced by the diffuse nature of the force-spreading, which is locally first-order [25].

Furthermore, because the tube deforms in the y-z plane, the confinement effect of the domain in this plane was verified. For simulations resulting in a deformed radius that is less than 70% of the domain lengths in y and z, these lengths are taken as $\sim 4.7R_0$. Doubling these lengths changes the circumferential strain by less than 0.15% and the flow rate by about 0.015% (for the baseline case in Fig. 7), which are deemed negligible. For higher vessel deformation, it is necessary to increase the lengths. Similar tests were done to verify that the results are not affected by the domain size at higher deformation.

3.1.2. Comparison against analytical theories

Next, the simulation results are compared against analytical theories for flow-induced inflation of a Hookean tube. First, two models are considered: a classical result from Fung based on the Law of Laplace (hereafter, LL), and a shell theory approach by Anand & Christov (hereafter, AC) [1,4]. In comparing against the numerical results, some features of these models need to be noted. In both models, the assumption of small deformation was utilized. Additionally, these models were derived by solving the solid and fluid mechanics separately, then coupling them by treating the fluid pressure as a load deforming the structure. The results represent an equilibrium between the pressure-induced deformation and the flow modified by the deformed shape. The two approaches differ in the radius used when calculating the circumferential stress in the vessel wall: the deformed radius R(x) in the Law of Laplace, and the undeformed radius R_0 in Anand & Christov. The pressure-radius relationships for the models are as follows:

Law of Laplace (LL):
$$R(x) = R_0 \left[1 - \frac{R_0}{E'h} P(x) \right]^{-1}, \tag{45}$$

Anand & Christov (AC):
$$R(x) = P(x) \left[\left(1 - v^2 \right) \frac{R_0^2}{Eh} \right] + R_0, \tag{46}$$

where E' is an "effective" 2D modulus which relates to the 3D modulus E by $E' = \frac{E}{1-\nu^2}$. This is consistent with a plane strain formulation [70], from which the surface modulus is written as $E_s = Eh = E'h(1-\nu^2)$ (see § 2.2). In both models, $\nu_s = \nu$, and the subscript s is dropped for brevity.

A second-order law of Laplace

To alleviate the limitation posed by the assumption of small deformation in the above models, we introduce a second-order correction to the law of Laplace as follows. We begin by writing the θ -component of the Green strain tensor in cylindrical coordinates (R, θ, x) in its full form as

$$\epsilon_{\theta} = \frac{v_R}{R_0} + \frac{1}{R_0} \frac{\partial v_R}{\partial \theta} + \frac{1}{2R_0^2} \left[\left(\frac{\partial v_R}{\partial \theta} \right)^2 + \left(\frac{\partial v_{\theta}}{\partial \theta} \right)^2 + \left(\frac{\partial v_x}{\partial \theta} \right)^2 - 2v_{\theta} \frac{\partial v_R}{\partial \theta} + 2v_R \frac{\partial v_{\theta}}{\partial \theta} + v_{\theta}^2 + v_R^2 \right], \tag{47}$$

where v is the wall displacement (following the notation of Heil, Pedley, and Hazel [14–17]) with radial component $v_R = R(x) - R_0$. Traditionally, the deformation is assumed both small and axisymmetric, and the higher-order terms are neglected. Eq. (47) then reduces to

$$\epsilon_{\theta} = \frac{v_R}{R_0}.\tag{48}$$

This form is used in both the AC model and the Law of Laplace.

Instead, the second-order theory retains the quadratic terms by foregoing the small-deformation assumption and only assuming axisymmetric deformation. With this assumption eq. (47) reduces to

$$\epsilon_{\theta} = \frac{v_R}{R_0} + \frac{v_R^2}{2R_0^2}. (49)$$

Following Hooke's law, the strain is expressed in terms of circumferential stress σ_{θ} as

$$\epsilon_{\theta} = \frac{\sigma_{\theta}}{E'},$$
 (50)

and, as in the Law of Laplace, the stress is further expressed in terms of pressure as

$$\sigma_{\theta} = \frac{P(x)R(x)}{h}.\tag{51}$$

Combining eqs. (49)–(51), we arrive at

$$2^{nd} \text{ order Law of Laplace:} R(x) = \frac{R_0^2 P(x)}{E'h} + \sqrt{\left(\frac{R_0^2 P(x)}{E'h}\right)^2 + R_0^2}. (52)$$

One may also recover the standard Law of Laplace by combining eqs. (48), (50) and (51). As discussed in [4], the Law of Laplace utilizes the small-deformation assumption in eq. (48) but not in eq. (51), thus "mixing" the deformed and undeformed frames of reference. This yields an inverse radius-pressure relationship, which diverges at moderate deformations, that does not appear when the second-order terms are retained. On the other hand, Anand & Christov's model avoids a divergent relationship by maintaining the small deformation assumption throughout, formulating the pressure load as

$$\sigma_{\theta} = \frac{P(x)R_0}{h}.\tag{53}$$

Combining eqs. (48), (50) and (53) yields the AC theory.

Now we can compare the prediction of R(x) from our numerical method against all three analytical theories as shown in Fig. 8. A few distinctions between the theories and the numerical setup must be kept in mind while comparing the results. In the numerical setup, the deformable segment is clamped at the ends, while in the theories both ends are free to distend. As such, for comparison of the radial displacement $R(x) - R_0$, only the deforming section downstream from the point of maximum distention is considered. Fig. 8(a) shows the radial displacement along the vessel length for varying pressure drop. As seen, at the smallest pressure drop considered, there is a strong agreement between the numerical result and all three theories because deformation is small. At higher pressure drops (with larger deformation), both the law of Laplace and AC deviate from the numerical prediction, while the second-order theory maintains very good agreement with the numerical prediction. Fig. 8(b) compares the centerline pressure, showing the same strong agreement between the numerical prediction and the second-order theory.

Fig. 8(c) shows the radial displacement against centerline pressure. In this, each theoretical curve becomes independent of the applied pressure drop. The second-order formula again shows excellent agreement with the numerical results even for very large deformation, while the law of Laplace and AC deviate on account of the small deformation assumption. Note that the law of Laplace overpredicts the numerical data while AC underpredicts. This is because in LL, as discussed previously, R(x) is reciprocal with P(x) and hence diverges at large pressure, as is evident from both eq. (45) and Fig. 8(c). In contrast, AC posits a linear radius-pressure relationship where the pressure acts only on the undeformed state (eq. (53)). At moderate deformation, this does not account for the full load on the structure, leading to the underprediction.

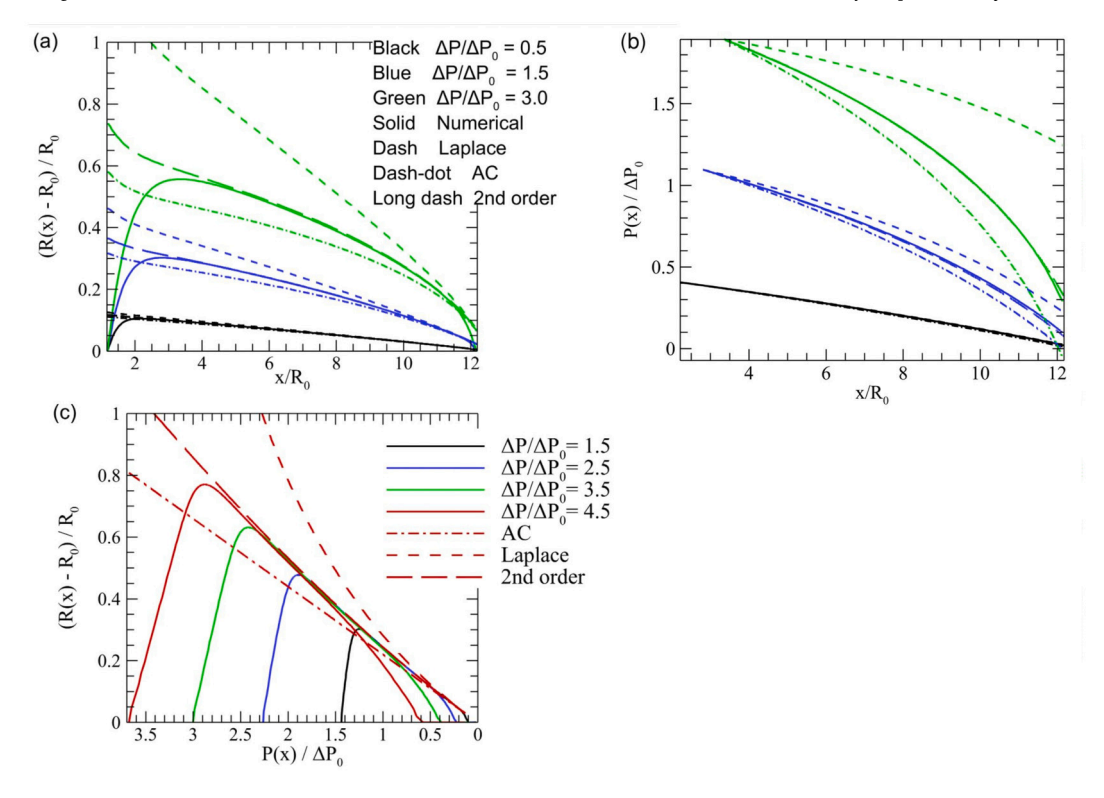


Fig. 8. Comparison of the numerical prediction against the analytical theories for a Hookean vessel, v = 0.5, $\varepsilon = 0.02$. In all figures, solid lines are the numerical prediction, dash line is the law of Laplace (eq. (45)), dash-dot is AC (eq. (46)), and long dash is the second-order formula (eq. (52)). (a) Radial displacement along the deformable segment for three different pressure drops $\frac{\Delta P}{\Delta P_0} = 0.5$ (black), 1.5 (blue), 3 (green). (b) Centerline pressure for the same cases. (c) Radial displacement versus centerline pressure for $\frac{\Delta P}{\Delta P_c} = 1.5$ (black), 2.5 (blue), 3.5 (green), 4.5 (red).

Further comparisons of the simulated results against the above theoretical models can be made using volume flow rate versus pressure drop. To obtain the flow rate Q, the Hagen-Poiseuille relation for flow in a rigid tube is assumed to hold locally at any axial

$$\frac{dP(x)}{dx} = -\frac{8\mu}{\pi R(x)^4} Q. \tag{54}$$

Using the expressions of R(x) for the different analytical theories, this equation can be integrated along x to obtain the pressure-flow rate relations. To mitigate the effects of the clamped ends in the present numerical setup, the integration is performed from the location of the maximum radial deformation $x = \tilde{x}$ to the end of the deformed segment $x = x_d$. Then, the theories yield:

Fung (using Law of Laplace):
$$Q = \frac{\pi R_0^3 E' h}{24\mu \left(x_d - \widetilde{x}\right)} \left\{ \left[1 - \overline{P}\left(\widetilde{x}\right)\right]^{-3} - \left[1 - \overline{P}\left(x_d\right)\right]^{-3} \right\},\tag{55}$$

AC:
$$Q = \frac{\pi R_0^3 E' h}{40\mu \left(x_d - \widetilde{x}\right)} \left\{ \left[1 + \overline{P}\left(\widetilde{x}\right)\right]^5 - \left[1 + \overline{P}\left(x_d\right)\right]^5 \right\},\tag{56}$$

$$Q = \frac{\pi R_0^3 E' h}{120\mu \left(x_d - \widetilde{x}\right)} \left\{ 15 \left(\overline{P}\left(\widetilde{x}\right) - \overline{P}\left(x_d\right)\right) - 20 \left[\left(\overline{P}\left(\widetilde{x}\right)^2 + 1\right)^{3/2} - \left(\overline{P}\left(x_d\right)^2 + 1\right)^{3/2} \right] + 24 \left[\left(\overline{P}\left(\widetilde{x}\right)^2 + 1\right)^{5/2} - \left(\overline{P}\left(x_d\right)^2 + 1\right)^{5/2} \right] + 40 \left(\overline{P}\left(\widetilde{x}\right)^3 - \overline{P}\left(x_d\right)^3\right) + 24 \left(\overline{P}\left(\widetilde{x}\right)^5 - \overline{P}\left(x_d\right)^5\right) \right\}$$

$$(57)$$

where $\overline{P}(x) = \frac{R_0}{E'h}P(x)$. To compare the numerical results and the theories, we consider the flow rate ratio Q/Q_0 where Q_0 is the flow rate in the undeformed vessel. Furthermore, the pressure drops from \tilde{x} to x_d are denoted by $\Delta \tilde{P}$ and $\Delta \tilde{P}_0$ for the deformed and the undeformed vessels, respectively. Fig. 9 compares Q/Q_0 versus $\Delta \widetilde{P}/\Delta \widetilde{P}_0$ for different values of deformability ε . As seen, at lower $\Delta \widetilde{P}/\Delta \widetilde{P}_0$ and

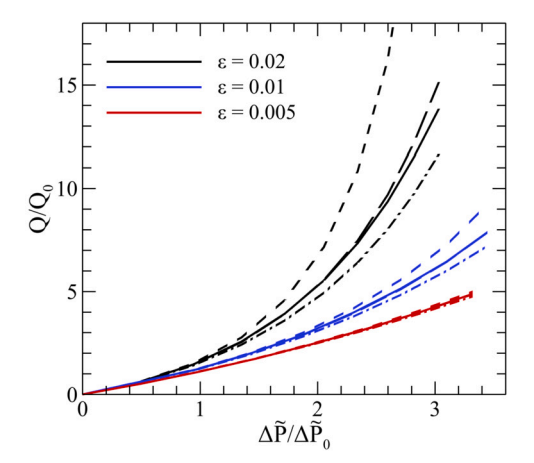


Fig. 9. Comparison of the numerical predicted pressure-flow rate data against the analytical theories for Hookean model, $\nu = 0.5$. The solid line is the numerical prediction, dash line is Fung's model derived using the Law of Laplace (eq. (55)), dash-dot is AC (eq. (56)), and long dash is the second-order formula (eq. (57)). For $\varepsilon = 0.005$ and 0.01, the second-order formula is indistinguishable from the numerical results.

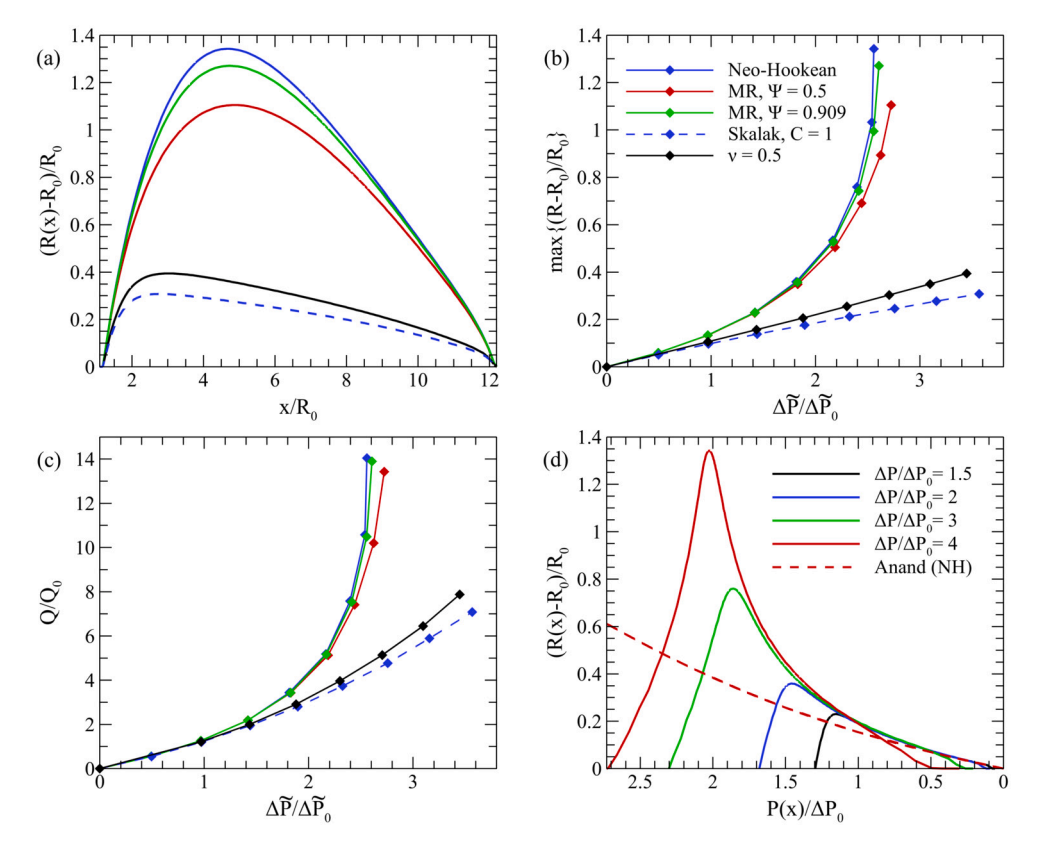


Fig. 10. Vessel inflation simulations using nonlinear constitutive models. For all cases $\varepsilon = 0.01$. (a) radial displacement along vessel length for a fixed $\frac{\Delta P}{\Delta P_0} = 4$. (b) Maximum displacement versus pressure drop. (c) Flow rate versus pressure drop. (d) Radial displacement versus centerline pressure for $\frac{\Delta P}{\Delta P_0} = 1.5$ (black), 2 (blue), 3 (green), 4 (red). The red dashed line is the model by Anand for a Neo-Hookean tube. For all plots except (d), the legend is in (b).

 ε , there is a strong agreement between the numerical prediction and all three analytical theories. At higher $\Delta \widetilde{P}/\Delta \widetilde{P}_0$ and ε , the second-order theory shows good agreement, while the law of Laplace overpredicts and AC underpredicts.

3.1.3. Nonlinear constitutive models

Next, we demonstrate the model's capability to consider vessels with nonlinear elastic behavior. The inflation simulations with Mooney-Rivlin, Neo-Hookean, and Skalak's models are compared with the Hookean model in Fig. 10. For the same applied pressure drop, the Neo-Hookean model shows the largest deformation, followed by the Mooney-Rivlin model for $\Psi < 1$, then the Hookean

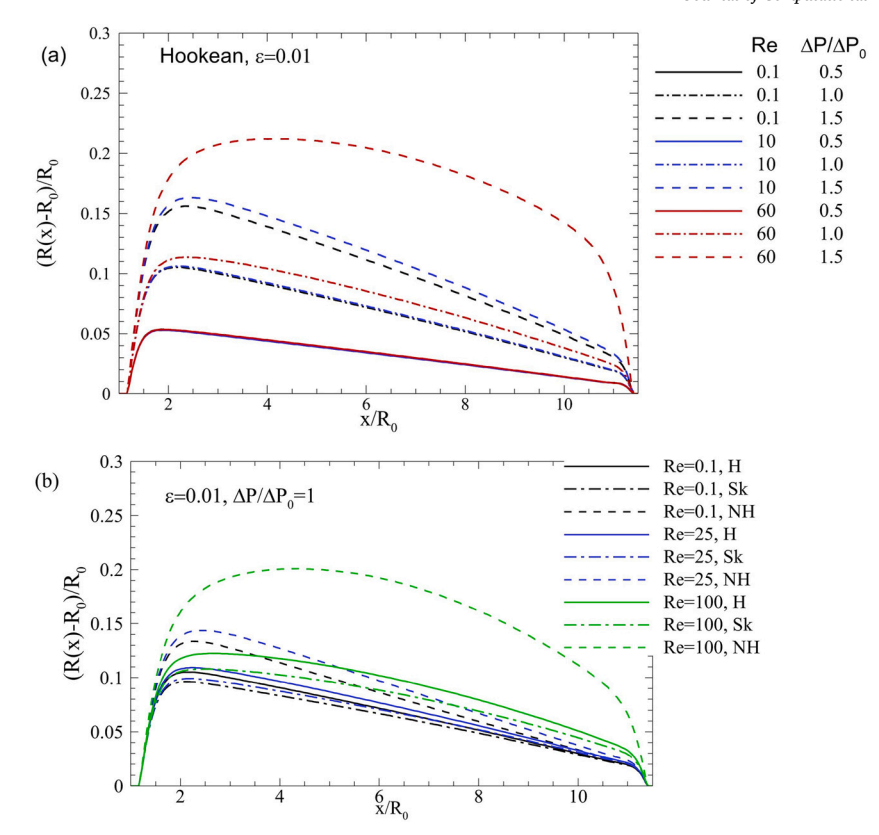


Fig. 11. Vessel inflation at finite inertia. Radial displacement along vessel axis for (a) Hookean model at $\varepsilon = 0.01$ under varying Re and pressure drop, and (b) for different constitutive models and varying Re.

model, while Skalak's model deforms the least. When varying the pressure drop, the Neo-Hookean and Mooney-Rivlin models quickly rise above the other models as the pressure drop increases, due to their strain softening behavior. For these models, the maximum deformation shows a diverging trend, as opposed to the linear trend for the Hookean model. Furthermore, the deformation increases with increasing Ψ on account of reduced tension (as noted in § 2.2), leading to the Neo-Hookean model showing the largest deformation. Flow rate versus pressure drop curves are shown in Fig. 10(c) and follow the same trend as the maximum displacement. Fig. 10(d) depicts the radius vs centerline pressure relationship for the Neo-Hookean tubes. The strong nonlinearity of the curve is again indicative of a strain softening material. A model by Anand for a Neo-Hookean tube is shown for reference [5], though it does not match the results well beyond small deformations as it assumes a long, slender tube and neglects fluid traction.

3.2. Inflation at higher inertia

Next, we demonstrate the methodology for vessel inflation at higher fluid inertia. In this section the total tube length is $L^* = 4\pi$, with section lengths $L^*_{inlet} = L^*_{outlet} = 1.18$, and $\check{L}^* = 10.2$. Fig. 11(a) shows the steady radial displacement of a Hookean tube for varying Re and applied pressure drop. At low pressure drops, Re has very little effect on vessel deformation, but as the pressure drop increases, significant differences appear. At higher Re, we observe much higher radial displacement, with a profile that deviates from the decreasing linear profiles of lower Re. Additionally, the location of maximum inflation moves downstream as Re increases.

Fig. 11(b) shows the effect of Re for the nonlinear constitutive models. As was the case at small inertia, the NH model shows maximum deformation, followed by Hookean and Skalak's models. Large differences between the different models are seen at the highest Re considered.

Numerical predictions at finite inertia can also be compared with the analytical theories. For this, in Fig. 12(a) the radial displacement versus axial pressure is shown. Like the low inertia case seen before, the AC theory underpredicts and the law of Laplace overpredicts, while the second-order formula agrees very well with the numerical data. This is to be expected, as the solid mechanics do not change between the high and low Re cases. One difference with the low inertia results is that pressure near the left end of the deforming segment rises much more rapidly. This happens because the dominance of the inertial effects over the viscous effects results in a higher pressure as the fluid velocity decreases due to area increase (i.e., Bernoulli's principle). Further comparison in terms of the flow rate versus pressure drop is shown in Fig. 12(b). In this case, in contrast to the radius vs pressure relationship, all three theories overpredict the flow rate to varying degrees. However, despite not including inertial terms in its derivation, the AC theory closely matches the data. Also plotted here is an extension to the AC theory for flows with finite inertia by Wang et al. [6], which underpredicts the results. A potential cause for this discrepancy is that, like the other theories, it assumes a parabolic velocity

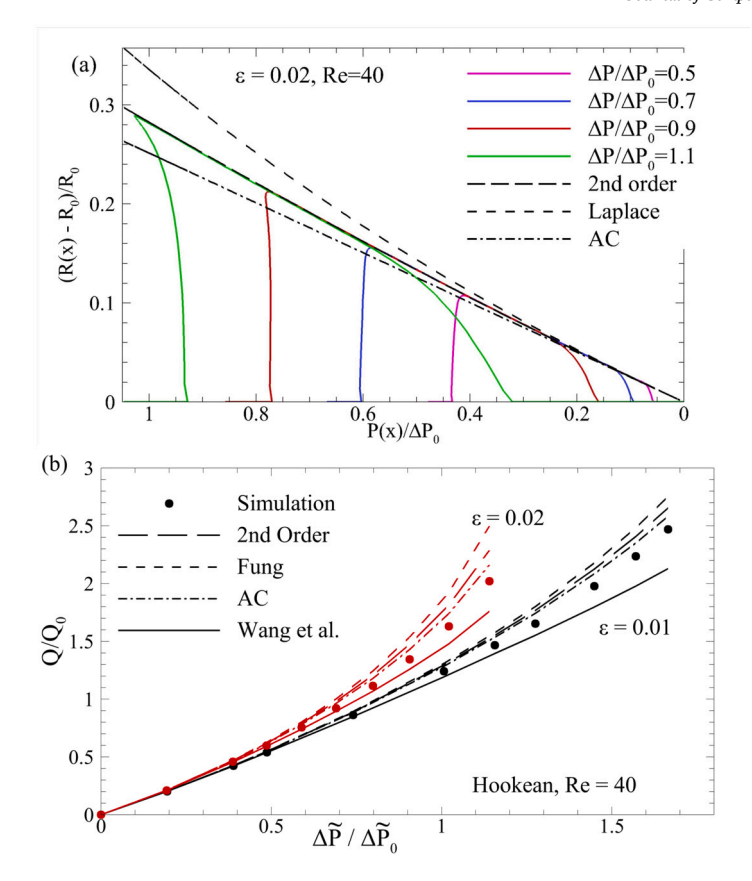


Fig. 12. Vessel inflation at finite inertia and comparison with analytical theories. (a) Radial displacement versus centerline pressure at Re = 40 for a Hookean vessel at different pressure drops. (b) Flow rate versus pressure drop.

profile at each cross section, which is not a good match for the simulation data. This assumption, when combined with the inertial effects, causes the underprediction.

3.2.1. Transient dynamics at finite inertia

At finite inertia, the tube inflation exhibits different transient behaviors that are complex but resolved by our method. These are demonstrated next. For moderate inertia and deformation, the inflation in response to a sudden application of pressure drop occurs via a damped oscillation before reaching a steady state. This is shown in Fig. 13(a) where the transient flow rate at the vessel inlet is plotted. As seen, the flow rate exhibits a damped oscillation, and the oscillation's amplitude and duration increase with increasing Re. The time-dependent vessel boundary is presented in Fig. 13(b) for one case which shows a complex shape evolution. Such oscillations arise due to the back-and-forth reflections of a pressure wave between the clamped ends that occurs at this higher inertia as predicted by our method and shown in Fig. 13(c).

At sufficiently high Re and ε , however, such oscillations sustain to become periodic as predicted by our model. Fig. 14 shows one example at Re = 50, $\varepsilon = 0.02$. Large variation in vessel shape and fluid velocity over time can be seen here. Several striking features can also be noted; first, within each period of oscillation the vessel shape and fluid velocity oscillate between the maximum and minimum. The minimum deformation is very close to the undeformed state with very little flow. Second, a recirculation region emerges near the end of the vessel during each oscillation period when deformation is large but disappears when deformation is small. The maximum inflation is noted near the end of the deforming segment, which is exactly opposite to what was observed for low inertia. This behavior is due to the recirculation region which causes a local increase in the internal pressure. The surface mesh remains smooth without any distortion even after several oscillation periods.

3.3. Collapsing vessels

Next, we demonstrate the capability of the methodology to simulate collapsing (or, buckling) vessels. This occurs when the vessel external pressure is greater than the internal pressure. These problems require no change to the simulation setup; only the bending resistance of the wall material is added (§ 2.4). Unless stated otherwise, we set $P_0^* = P_{ext}^* = 0$, $P_L = -\Delta P_0$, and $\varepsilon = 0.005$. The undeformed tube has a circular cross-section. Results for small inertia are presented first, followed by higher inertia.

Mesh resolution tests were also performed for collapsing vessels by increasing the Eulerian points in each direction by a factor of 2 and 4, and the surface triangular elements by a factor of 2^2 and 4^2 . For the two finer resolutions, the maximum difference in the

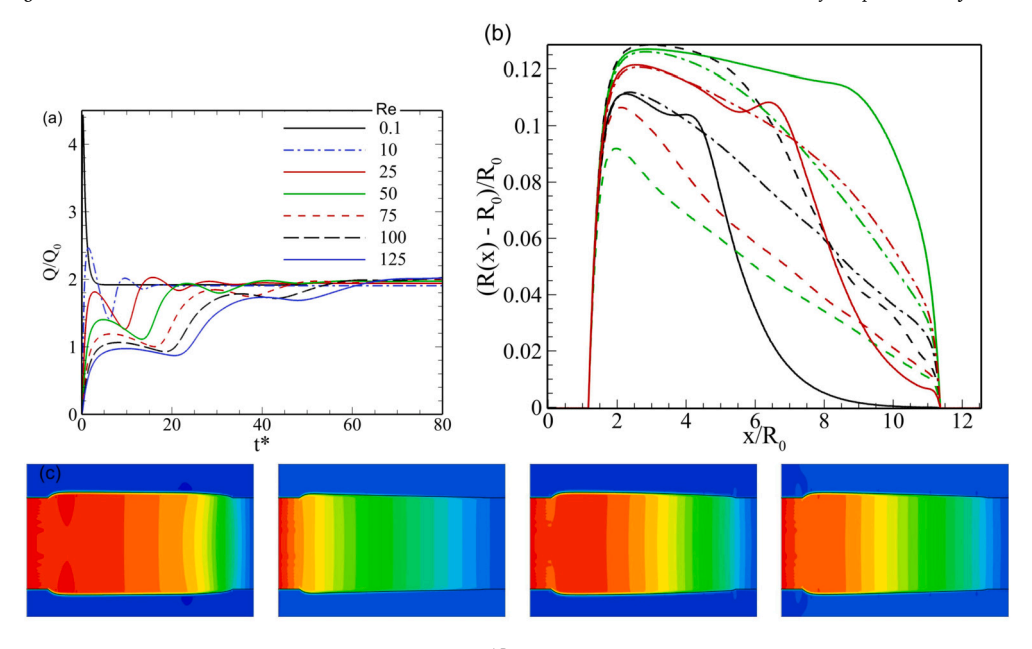


Fig. 13. Damped oscillations at finite Re. Parameters: Hookean tube, $\epsilon = 0.01$, $\frac{\Delta P}{\Delta P_0} = 1$. (a) Time-dependent flow rate at different Re. (b) Time-dependent vessel shape shown using the radial displacement for Re = 125. The first inflation phase is represented by the solid curves, followed by a deflation phase shown using the dash lines, and the next inflation phase by the dash-dot lines. For each phase, black, red and green curves represent three time instances in progression. (c) Sequence showing pressure contours moving back-and-forth for the case in (b).

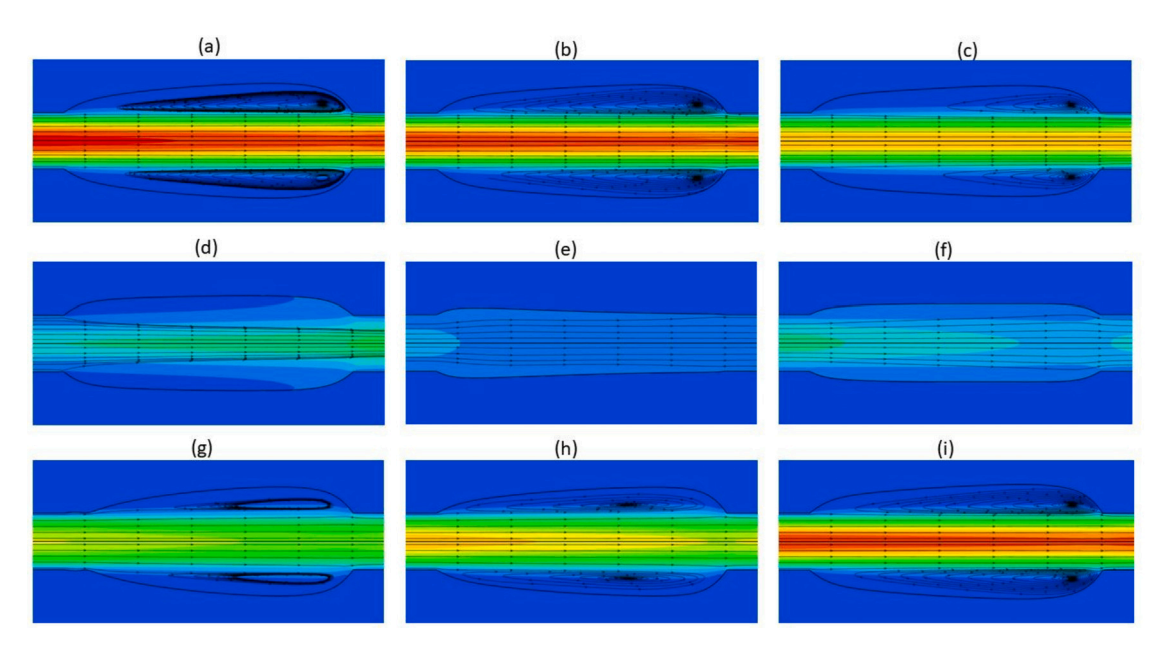


Fig. 14. Inflation at higher Re and ε showing sustained flow and shape oscillation and recirculation. Hookean tube, Re = 50, $\varepsilon = 0.02$. (a)–(i) show one oscillation period.

radial displacement is 0.1%. Therefore, we select the intermediate resolution for which the Eulerian mesh size is $0.052R_0$, and the undeformed surface element area is $\sim 2 \times 10^{-3} R_0^2$.

3.3.1. Collapsing vessels at small inertia

Here we fix Re = 0.1. By varying P_L , bending modulus B, and vessel length, different patterns of collapsed shapes can be obtained. Such steady shapes as predicted by our simulations are shown in Fig. 15. Under specific parameter ranges, well-characterized shapes are predicted as shown. These shapes are characterized by, respectively, two or more "lobes" and classically referred to as buckling modes of n = 2, 3, etc. as in Timoshenko and Gere [9]. It should be noted that, in most cases, the tube naturally buckles into specific

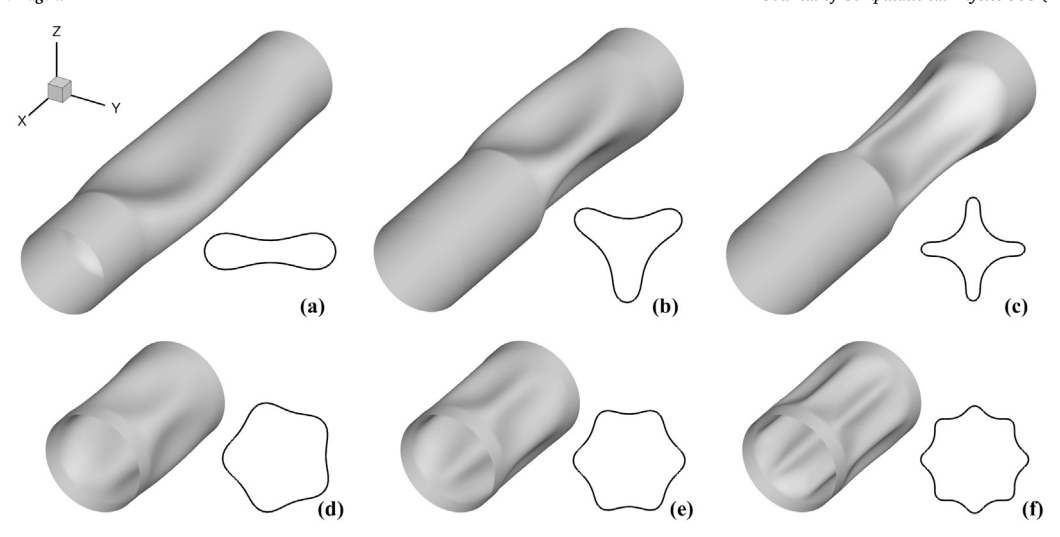


Fig. 15. Shapes of collapsed vessels under varying parameters. (a) to (f) represent different modes characterized by n = 2, 3, ..., 6 and 8 "lobes", respectively. For each case, the 3D view and the tube perimeter at maximum collapsed location are shown.

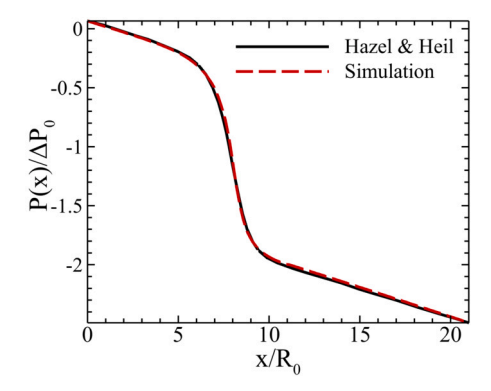


Fig. 16. Centerline pressure in a collapsed tube. The solid black line is from Hazel and Heil [14], while the red dashed line is our simulation data. The prescribed pressures at the inlet and outlet are $\frac{P_0}{A_0} = 0.065$ and $\frac{P_L}{\Delta P_0} = -2.493$, respectively. The external pressure is kept at 0. Parameters: $L^* = 21$; $L^*_{inlet} = 1$; $L^* = L^*_{outlet} = 10$; $\epsilon = 2.5 \times 10^{-4}$; $B = 1.953 \times 10^{-3}$; v = 0.49.

modes for a given parameter set. Also note that the simulations are time-dependent; only the final steady shapes are shown in the figure.

Collapse into mode 2, or a "dumbbell" shape, has been well characterized in the literature on flows through collapsing tubes [8]. As seen in Fig. 15(a), the tube's shape gradually buckles starting at the upstream end and moving downstream, becoming narrowest far downstream before rapidly adjusting to the undeformed (circular) rigid outlet. These features have been observed in many classical experiments with the Starling resistor [8]. Fig. 16 shows the corresponding pressure distribution along the centerline, which follows a linear trend in the circular sections of the vessel corresponding to Poiseuille flow, but rapidly decreases in the most collapsed region. In addition to our simulation results, also shown in Fig. 16 is a steady computational result from Hazel and Heil [14]. Despite the numerous differences between the two approaches (flow-controlled vs pressure-controlled experiment, steady vs unsteady flow, small vs large strain solid mechanics models, etc.), the two curves show excellent agreement.

Beyond such single-mode buckling, our methodology can simulate highly complex buckled shapes, as demonstrated by an example in Fig. 17, which are not characterized by any single mode. Even with such an extremely collapsed, complex shape, the methodology provides a final stable shape and flow. The thin folds on the vessel surface as seen in the figure are well-resolved without any significant distortion in the surface mesh. Note that such complex buckling occurs spontaneously without any application of forced perturbation.

We further simulated collapsing tubes with different constitutive models (Hookean, Neo-Hookean, and Skalak's models). We find that these constitutive models make no significant change in the vessel shape, as shown in Fig. 18, since buckling is primarily determined by bending resistance.

3.3.2. Collapsing vessels at moderate inertia

We further considered collapsing vessel simulations at higher inertia. Figs. 19 and 20 compare the results for different Re for modes n = 3 and 4, respectively. The qualitative nature of the vessel shape remains independent of Re for the range considered,

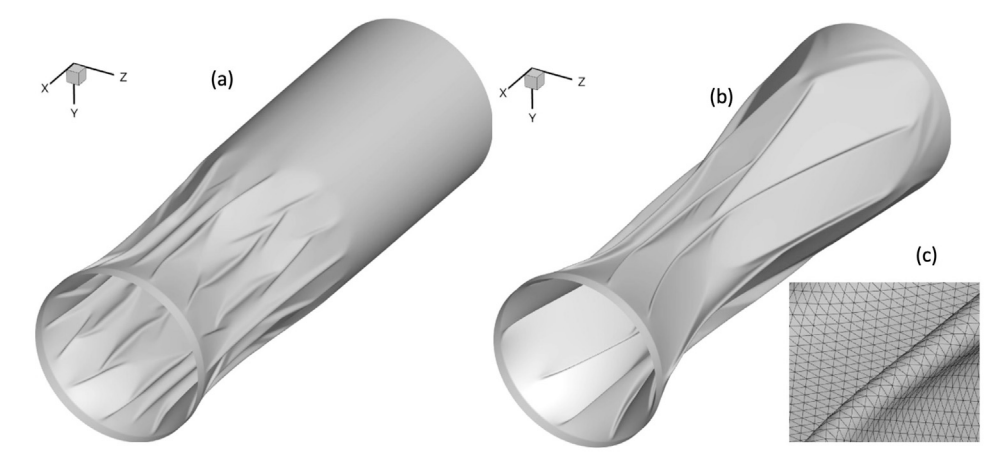


Fig. 17. Prediction of a highly complex buckled shape. (a), (b) instantaneous images at an initial and a later (near-completion) time during the buckling process. (c) Close-up of surface mesh on the vessel near a surface fold for the instant in (b). Parameters: Hookean model, $L^* = 2\pi$, $\check{L}^* = 6$, $L^*_{inlet} = L^*_{outlet} = 0.142$, Eulerian resolution: $570 \times 237 \times 236$, Lagrangian elements: 499000, $B = 10^{-6}$.

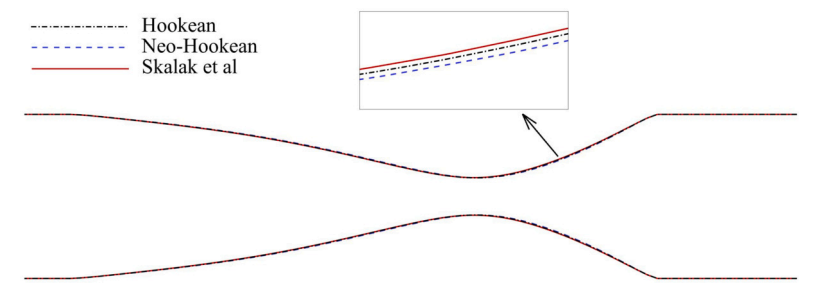


Fig. 18. Influence of wall material constitutive models on buckled shapes. Shown here is mode n = 2.

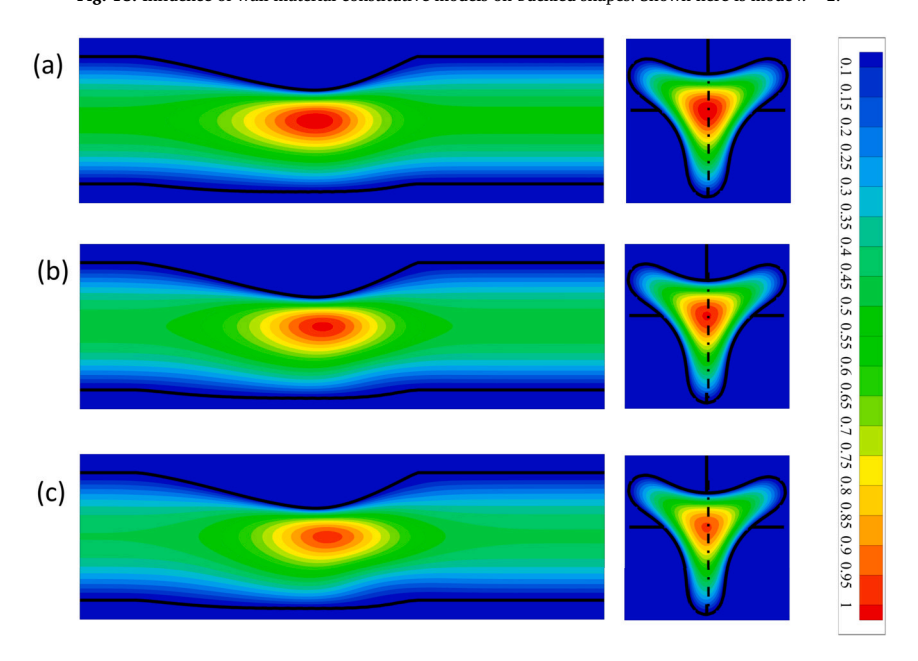


Fig. 19. Finite Re effect on collapsing tube for mode n = 3. Vessel boundary and streamwise velocity contours are shown for Re = 0.1, 10, 20 in (a), (b), and (c), respectively.

but a small increase in deformation, as characterized by more reduction in the cross-sectional area, with increasing Re is observed for all modes. This is consistent with the findings in [14]. Velocity contours are also qualitatively similar for different Re, but the streamwise velocity decreases on account of the area reduction at higher Re, which increases the flow resistance.

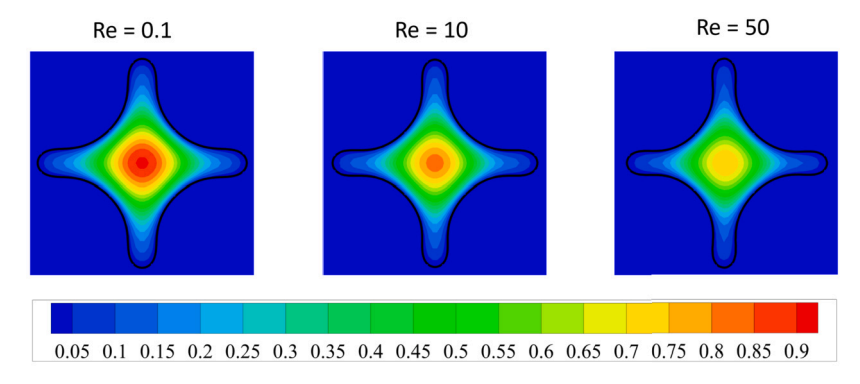


Fig. 20. Finite Re effect on collapsing tube for mode n = 4. Vessel cross-sectional boundary at the location of maximum deformation and streamwise velocity contours are shown for Re = 0.1, 10.50.

4. Conclusion

In this article, we have developed and demonstrated a computational method capable of modeling 3D, transient, flow-induced deformation of thin, highly compliant, hyperelastic vessels conveying viscous, inertial fluid. It combines finite volume and spectral methods for fluid motion, a finite element method for the structural mechanics of the vessel wall, and IBM for two-way coupling between the deforming wall and fluid. Specifically, a hybrid of the continuous forcing and ghost node methodologies has been developed for the full FSI that capitalizes on the strengths of each. This method avoids the problems encountered with the continuous forcing methods, namely, the issue of instability associated with crumpling and excessive stretching of an elastic surface, and the inaccuracy in the streamwise flow very close to the vessel wall. It also avoids the need for domain remeshing as required in the iterative and partitioned approaches. The method can uniformly consider vessel extension and collapse in the same setup. Very large inflation (~ 150%), transient deformation, complex flow features (transient recirculation), and highly complex buckling shapes are well resolved by this method. The vessel wall can follow linear or nonlinear (strain softening and hardening) material models, and the fluid inertia can vary over a wide range.

In addition to the hybrid method, we have also presented a fast, parallelizable method for identifying GNs for an arbitrarily deforming geometry, which allows reidentification in each timestep without significant computational overhead. Reidentification of nodes and boundary intercepts is required in any GN problem with moving boundaries, and it can be an expensive process. Specific methods are not often discussed. The presented method is applicable to any moving boundary problem involving GNs to reduce the computation time.

The transition from a rigid segment (solved using the ghost-node method) to a deforming segment (solved using the hybrid method) requires special treatment, which is also discussed. The singularity at the transition point is well resolved, yielding a smooth vessel surface contour with no mesh distortion. As such, the current method is readily applicable to vessels or surfaces that have multiple rigid and deforming segments.

The specific application of the Helfrich bending energy model to the problem of collapsing vessels as presented here is also novel as it has not been considered previously. As discussed in § 1, the prior full FSI modeling studies on collapsing vessels used shell theories, which inherently include bending resistance. To our knowledge, the energy-based variational principle for bending has not been applied to collapsing vessels previously.

Additionally, a second-order correction to the well-known law of Laplace has been developed, as well as a corresponding flow rate-pressure drop relationship, for an inflating Hookean tube. At large inflation, this theory shows significantly closer agreement with our simulation data compared to existing small deformation models.

The methodology revealed interesting dynamics of deforming vessels. With the inflation at low fluid inertia, the flow and vessel achieve a steady state with larger deformation near the entrance and reduced deformation towards the exit. At moderate inertia, the vessel and flow can exhibit either a damped oscillation before reaching a steady state or a periodic oscillation even though the boundary conditions are held steady. The back-and-forth movement of the pressure wave is also resolved for such time-dependent cases. Furthermore, at moderate inertia, the inflation is higher near the vessel exit than near the entrance, in stark contrast to the low inertia cases, which is the result of flow recirculation developing near the exit. For the collapsing vessel simulations, well-defined shapes with different buckling modes (such as, dumbbell and multi-lobes) as obtained in the classic work of Timoshenko, as well as highly complex buckling with fine surface folds are predicted by our model. Such varied shapes (regular or complex) occur naturally just under the application of a negative transmural pressure and without any artificial perturbing force.

The main limitation of this method is that it neglects axial motion. As such, this method is not suitable for problems where significant axial deformation is expected, such as axial buckling, or extremely large balloon-like deformation. In problems without such deformations, allowing axial motion would allow minor adjustments between adjacent Lagrangian nodes, such that the stresses in the finite elements will somewhat equilibrate with their neighbors. Physically, this corresponds to adjacent differential material fibers adjusting to similar lengths, yielding the lowest energy configuration of the tube. Such changes are expected to be minor within the scope of problems considered here. Under physiological conditions where blood vessels are surrounded by tissue, the axial stretch is negligible compared to radial stretch. Prior and current biological data present only the radial stretch; we have not found

data on axial stretching of blood vessels intact within a tissue. The wall shear stress acts to deform the endothelial cells; we have not come across papers where this was shown to axially stretch blood vessels. Early theoretical and numerical models which are cited here also consider radial stretch. Thus, having blood flow as the application in mind, it is appropriate to neglect axial stretch. Even though the displacement is restricted to 2D planes, the structural mechanics problem is fully 3D. Beyond this restriction, note also that the force spreading and velocity interpolation by discrete delta function are, in the problems reported here, less efficient than the computations associated with the GN method. As such, in cases with small deformations which are well described by lower order models for the solid mechanics, one might achieve greater computational efficiency by opting for a purely GN approach with one-way coupled interaction, such as in [48].

The versatility of the current methodology lends its applicability to multiple problems. Physiologically realistic constitutive models can be used to represent blood vessels, lung airways, or lymphatic vessels. Further, the FEM framework used here can incorporate viscoelastic surfaces. Pulsatile flow conditions can also be easily considered. The flow of blood as a suspension of deformable red blood cells through the compliant vessel can be readily modeled, as well as flows in compliant microfluidic channels. Finally, the methodology is not just limited to straight vessels, but can be applied to vessels with complex geometry, such as curves and bifurcations, with deforming walls, as long as the axial stretch remains negligible as in case of microvascular blood flow.

CRediT authorship contribution statement

Oleksander Krul: Data curation, Investigation, Methodology, Software, Validation, Writing – original draft. **Prosenjit Bagchi:** Conceptualization, Funding acquisition, Project administration, Supervision, Writing – review & editing.

Declaration of competing interest

The authors declare that they have no known competing financial interests or personal relationships that could have appeared to influence the work reported in this paper.

Data availability

Data will be made available on request.

Declaration of generative AI and AI-assisted technologies in the writing process

No generative AI or assisted technology was used to prepare the manuscript.

Acknowledgement

This work was supported by a grant from the National Science Foundation (CBET 1922839).

Computational resources at Pittsburgh Supercomputing Center, Texas Advanced Computing Center, and Purdue University through ACCESS, and at Rutgers University are acknowledged.

References

- [1] Y.C. Fung, Biomechanics: Circulation, Springer New York, New York, NY, 1997.
- [2] T. Gervais, J. El-Ali, A. Günther, K.F. Jensen, Flow-induced deformation of shallow microfluidic channels, Lab Chip 6 (4) (2006) 500–507, https://doi.org/10.1039/B513524A.
- [3] S. Rubinow, J.B. Keller, Flow of a viscous fluid through an elastic tube with applications to blood flow, J. Theor. Biol. 35 (2) (1972) 299–313, https://doi.org/10.1016/0022-5193(72)90041-0.
- [4] V. Anand, I.C. Christov, Revisiting steady viscous flow of a generalized Newtonian fluid through a slender elastic tube using shell theory, J. Appl. Math. Mech. 101 (2) (Feb. 2021), https://doi.org/10.1002/zamm.201900309, arXiv:1810.05155.
- [5] V. Anand, A catalog of pressure and deformation profile for thin walled hyperelastic tubes conveying inertialess flow and undergoing large deformation, Thin-Walled Struct. 193 (2023) 111216, https://doi.org/10.1016/j.tws.2023.111216.
- [6] X. Wang, S.D. Pande, I.C. Christov, Flow rate–pressure drop relations for new configurations of slender compliant tubes arising in microfluidics experiments, Mech. Res. Commun. 126 (2022) 104016, https://doi.org/10.1016/j.mechrescom.2022.104016.
- [7] J.H. Olsen, A.H. Shapiro, Large-amplitude unsteady flow in liquid-filled elastic tubes, J. Fluid Mech. 29 (3) (1967) 513–538, https://doi.org/10.1017/ S0022112067001004.
- [8] J.B. Grotberg, O.E. Jensen, Biofluid mechanics in flexible tubes, Annu. Rev. Fluid Mech. 36 (1) (2004) 121–147, https://doi.org/10.1146/annurev.fluid.36. 050802.121918.
- [9] S. Timoshenko, J.M. Gere, Theory of Elastic Stability, 2nd edition, Dover Publications, Mineola, N.Y, 2009, originally published: McGraw Hill Book, New York, 1961.
- [10] T. Pedley, X. Luo, Modelling flow and oscillations in collapsible tubes, Theor. Comput. Fluid Dyn. 10 (1-4) (1998) 277-294, https://doi.org/10.1007/s001620050064.
- [11] T.J. Pedley, D. Pihler-Puzović, Flow and oscillations in collapsible tubes: physiological applications and low-dimensional models, Sadhana 40 (3) (2015) 891–909, https://doi.org/10.1007/s12046-015-0363-9.
- [12] A.H. Shapiro, Steady flow in collapsible tubes, J. Biomech. Eng. 99 (3) (1977) 126-147, https://doi.org/10.1115/1.3426281.
- [13] O.E. Jensen, T.J. Pedley, The existence of steady flow in a collapsed tube, J. Fluid Mech. 206 (1989) 339–374, https://doi.org/10.1017/S0022112089002326.
- [14] A.L. Hazel, M. Heil, Steady finite-Reynolds-number flows in three-dimensional collapsible tubes, J. Fluid Mech. 486 (2003) 79–103, https://doi.org/10.1017/ S0022112003004671.

- [15] M. Heil, Stokes flow in an elastic tube—a large-displacement fluid-structure interaction problem, Int. J. Numer. Methods Fluids 28 (2) (1998) 243–265, https://doi.org/10.1002/(SICI)1097-0363(19980815)28:2<243::AID-FLD711>3.0.CO:2-U.
- [16] M. Heil, Stokes flow in collapsible tubes: computation and experiment, J. Fluid Mech. 353 (1997) 285-312, https://doi.org/10.1017/S0022112097007490.
- [17] M. Heil, T.J. Pedley, Large post-buckling deformations of cylindrical shells conveying viscous flow, J. Fluids Struct. 10 (6) (1996) 565–599, https://doi.org/10.1006/jfls.1996.0039.
- [18] S. Zhang, X. Luo, Z. Cai, Three-dimensional flows in a hyperelastic vessel under external pressure, Biomech. Model. Mechanobiol. 17 (4) (2018) 1187–1207, https://doi.org/10.1007/s10237-018-1022-y.
- [19] B.E. Griffith, N.A. Patankar, Immersed methods for fluid-structure interaction, Annu. Rev. Fluid Mech. 52 (1) (2020) 421–448, https://doi.org/10.1146/annurev-fluid-010719-060228.
- [20] Z. Bai, L. Zhu, 3D simulation of a viscous flow past a compliant model of arteriovenous-graft annastomosis, Comput. Fluids 181 (2019) 403–415, https://doi.org/10.1016/j.compfluid.2019.02.006.
- [21] J. Teran, L. Fauci, M. Shelley, Peristaltic pumping and irreversibility of a Stokesian viscoelastic fluid, Phys. Fluids 20 (7) (2008) 073101, https://doi.org/10. 1063/1.2963530.
- [22] Y. Kim, Y. Park, S. Lim, 3D simulations of blood flow dynamics in compliant vessels: normal, aneurysmal, and stenotic arteries, Commun. Comput. Phys. 19 (5) (2016) 1167–1190, https://doi.org/10.4208/cicp.scpde14.20s.
- [23] R. Mittal, G. Iaccarino, Immersed boundary methods, Annu. Rev. Fluid Mech. 37 (1) (2005) 239-261, https://doi.org/10.1146/annurev.fluid.37.061903.175743.
- [24] C.S. Peskin, Flow patterns around heart valves: a numerical method, J. Comput. Phys. 10 (2) (1972) 252-271, https://doi.org/10.1016/0021-9991(72)90065-4.
- [25] C.S. Peskin, The immersed boundary method, Acta Numer. 11 (2002) 479-517, https://doi.org/10.1017/S0962492902000077.
- [26] A. Yazdani, P. Bagchi, Influence of membrane viscosity on capsule dynamics in shear flow, J. Fluid Mech. 718 (2013) 569–595, https://doi.org/10.1017/jfm. 2012.637.
- [27] Z. Bai, L. Zhu, Simulation of blood flow past a distal arteriovenous-graft anastomosis at low Reynolds numbers, Phys. Fluids 31 (9) (2019) 091902, https://doi.org/10.1063/1.5099635.
- [28] R.P. Beyer, A computational model of the cochlea using the immersed boundary method, J. Comput. Phys. 98 (1) (1992) 145–162, https://doi.org/10.1016/0021-9991(92)90180-7.
- [29] C. Cockerham Vesier, A.P. Yoganathan, A computer method for simulation of cardiovascular flow fields: validation of approach, J. Comput. Phys. 99 (2) (1992) 271–287, https://doi.org/10.1016/0021-9991(92)90207-F.
- [30] C. Tang, L. Zhu, G. Akingba, X.-Y. Lu, Viscous flow past a collapsible channel as a model for self-excited oscillation of blood vessels, J. Biomech. 48 (10) (2015) 1922–1929, https://doi.org/10.1016/j.jbiomech.2015.04.011.
- [31] G. Tryggvason, B. Bunner, A. Esmaeeli, D. Juric, N. Al-Rawahi, W. Tauber, J. Han, S. Nas, Y.-J. Jan, A front-tracking method for the computations of multiphase flow, J. Comput. Phys. 169 (2) (2001) 708–759, https://doi.org/10.1006/jcph.2001.6726.
- [32] X. Li, K. Sarkar, Front tracking simulation of deformation and buckling instability of a liquid capsule enclosed by an elastic membrane, J. Comput. Phys. 227 (10) (2008) 4998–5018, https://doi.org/10.1016/j.jcp.2008.01.034.
- [33] W.-X. Huang, C.B. Chang, H.J. Sung, Three-dimensional simulation of elastic capsules in shear flow by the penalty immersed boundary method, J. Comput. Phys. 231 (8) (2012) 3340–3364, https://doi.org/10.1016/j.jcp.2012.01.006.
- [34] A. Yazdani, P. Bagchi, Three-dimensional numerical simulation of vesicle dynamics using a front-tracking method, Phys. Rev. E 85 (5) (2012) 056308, https://doi.org/10.1103/PhysRevE.85.056308.
- [35] P. Balogh, P. Bagchi, A computational approach to modeling cellular-scale blood flow in complex geometry, J. Comput. Phys. 334 (2017) 280–307, https://doi.org/10.1016/j.jcp.2017.01.007.
- [36] E.J. Campbell, P. Bagchi, A computational model of amoeboid cell swimming, Phys. Fluids 29 (10) (2017) 101902, https://doi.org/10.1063/1.4990543.
- [37] D. Yoon, R. Mishra, D. You, Study of red blood cells and particles in stenosed microvessels using coupled discrete and continuous forcing immersed boundary methods, Phys. Fluids 35 (7) (2023) 071902, https://doi.org/10.1063/5.0152014.
- [38] Y. Kim, S. Lim, S.V. Raman, O.P. Simonetti, A. Friedman, Blood flow in a compliant vessel by the immersed boundary method, Ann. Biomed. Eng. 37 (5) (2009) 927–942, https://doi.org/10.1007/s10439-009-9669-2.
- [39] W. Lee, Y. Kim, C.S. Peskin, S. Lim, A novel computational approach to simulate microswimmers propelled by bacterial flagella, Phys. Fluids 33 (11) (2021) 111903, https://doi.org/10.1063/5.0069343.
- [40] Y. Kim, C.S. Peskin, A penalty immersed boundary method for a rigid body in fluid, Phys. Fluids 28 (3) (2016) 033603, https://doi.org/10.1063/1.4944565.
- [41] J. Mohd-Yusof, Combined Immersed-Boundary/B-Spline Methods for Simulations of Flow in Complex Geometries, Annual Research Briefs, Center for Turbulence Research, 1997, pp. 317–327.
- [42] R. Verzicco, J. Mohd-Yusof, P. Orlandi, D. Haworth, Large eddy simulation in complex geometric configurations using boundary body forces, AIAA J. 38 (3) (2000) 427–433, https://doi.org/10.2514/2.1001.
- [43] G. Pedrizzetti, F. Domenichini, Flow-driven opening of a valvular leaflet, J. Fluid Mech. 569 (2006) 321, https://doi.org/10.1017/S002211200600303X.
- [44] J. Mikhal, B.J. Geurts, Development and application of a volume penalization immersed boundary method for the computation of blood flow and shear stresses in cerebral vessels and aneurysms, J. Math. Biol. 67 (6–7) (2013) 1847–1875, https://doi.org/10.1007/s00285-012-0627-5.
- [45] S. Mirfendereski, J.S. Park, Direct numerical simulation of a pulsatile flow in a stenotic channel using immersed boundary method, Eng. Rep. 4 (1) (2022) e12444, https://doi.org/10.1002/eng2.12444.
- [46] R. Mittal, H. Dong, M. Bozkurttas, F. Najjar, A. Vargas, A. von Loebbecke, A versatile sharp interface immersed boundary method for incompressible flows with complex boundaries, J. Comput. Phys. 227 (10) (2008) 4825–4852, https://doi.org/10.1016/j.jcp.2008.01.028.
- [47] R. Mittal, J.H. Seo, V. Vedula, Y.J. Choi, H. Liu, H.H. Huang, S. Jain, L. Younes, T. Abraham, R.T. George, Computational modeling of cardiac hemodynamics: current status and future outlook, J. Comput. Phys. 305 (2016) 1065–1082, https://doi.org/10.1016/j.jcp.2015.11.022.
- [48] Z. Wang, J.H. Seo, R. Mittal, Mitral valve regurgitation murmurs—insights from hemoacoustic computational modeling, Fluids 7 (5) (2022) 164, https://doi.org/10.3390/fluids7050164.
- [49] F.-B. Tian, H. Dai, H. Luo, J.F. Doyle, B. Rousseau, Fluid-structure interaction involving large deformations: 3D simulations and applications to biological systems, J. Comput. Phys. 258 (2014) 451–469, https://doi.org/10.1016/j.jcp.2013.10.047.
- [50] J. Boustani, M.F. Barad, C.C. Kiris, C. Brehm, An immersed boundary fluid-structure interaction method for thin, highly compliant shell structures, J. Comput. Phys. 438 (2021) 110369, https://doi.org/10.1016/j.jcp.2021.110369.
- [51] M. Uhlmann, An immersed boundary method with direct forcing for the simulation of particulate flows, J. Comput. Phys. 209 (2) (2005) 448–476, https://doi.org/10.1016/j.jcp.2005.03.017.
- [52] W.-P. Breugem, A second-order accurate immersed boundary method for fully resolved simulations of particle-laden flows, J. Comput. Phys. 231 (13) (2012) 4469–4498, https://doi.org/10.1016/j.jcp.2012.02.026.
- [53] E.H. Dill, Continuum Mechanics: Elasticity, Plasticity, Viscoelasticity, 1st edition, CRC Press, 2006.
- [54] C. Pozrikidis (Ed.), Modeling and Simulation of Capsules and Biological Cells, Chapman & Hall/CRC Mathematical Biology & Medicine Series, vol. 2, Chapman & Hall/CRC, Boca Raton, FL, 2003.
- [55] D. Barthès-Biesel, J.M. Rallison, The time-dependent deformation of a capsule freely suspended in a linear shear flow, J. Fluid Mech. 113 (1) (1981) 251, https://doi.org/10.1017/S0022112081003480.

- [56] D. Barthès-Biesel, A. Diaz, E. Dhenin, Effect of constitutive laws for two-dimensional membranes on flow-induced capsule deformation, J. Fluid Mech. 460 (2002) 211–222, https://doi.org/10.1017/S0022112002008352.
- [57] R. Skalak, A. Tozeren, R. Zarda, S. Chien, Strain energy function of red blood cell membranes, Biophys. J. 13 (3) (1973) 245–264, https://doi.org/10.1016/S0006-3495(73)85983-1.
- [58] S. Shrivastava, J. Tang, Large deformation finite element analysis of non-linear viscoelastic membranes with reference to thermoforming, J. Strain Anal. Eng. Des. 28 (1) (1993) 31–51. https://doi.org/10.1243/03093247V281031.
- [59] O.-Y. Zhong-can, W. Helfrich, Bending energy of vesicle membranes: general expressions for the first, second, and third variation of the shape energy and applications to spheres and cylinders, Phys. Rev. A 39 (10) (1989) 5280–5288, https://doi.org/10.1103/PhysRevA.39.5280.
- [60] A. Guckenberger, S. Gekle, Theory and algorithms to compute Helfrich bending forces: a review, J. Phys. Condens. Matter 29 (20) (2017) 203001, https://doi.org/10.1088/1361-648X/aa6313.
- [61] S. Petitjean, A survey of methods for recovering quadrics in triangle meshes, ACM Comput. Surv. 34 (2) (2002) 211–262, https://doi.org/10.1145/508352. 508354.
- [62] G. Xu, Convergence of discrete Laplace-Beltrami operators over surfaces, Comput. Math. Appl. 48 (3) (2004) 347–360, https://doi.org/10.1016/j.camwa.2004. 05.001.
- [63] L. Zhu, C.S. Peskin, Simulation of a flapping flexible filament in a flowing soap film by the immersed boundary method, J. Comput. Phys. 179 (2) (2002) 452–468. https://doi.org/10.1006/jcph.2002.7066.
- [64] T. Krüger, M. Gross, D. Raabe, F. Varnik, Crossover from tumbling to tank-treading-like motion in dense simulated suspensions of red blood cells, Soft Matter 9 (37) (2013) 9008–9015, https://doi.org/10.1039/C3SM51645H.
- [65] T. Krüger, F. Varnik, D. Raabe, Efficient and accurate simulations of deformable particles immersed in a fluid using a combined immersed boundary lattice Boltzmann finite element method, Comput. Math. Appl. 61 (12) (2011) 3485–3505, https://doi.org/10.1016/j.camwa.2010.03.057.
- [66] H.-Y. Chang, X. Li, H. Li, G.E. Karniadakis, MD/DPD multiscale framework for predicting morphology and stresses of red blood cells in health and disease, PLoS Comput. Biol. 12 (10) (2016) e1005173, https://doi.org/10.1371/journal.pcbi.1005173.
- [67] H. Choi, P. Moin, Effects of the computational time step on numerical solutions of turbulent flow, J. Comput. Phys. 113 (1) (1994) 1–4, https://doi.org/10. 1006/jcph.1994.1112.
- [68] R. Mittal, S. Balachandar, Direct numerical simulation of flow past elliptic cylinders, J. Comput. Phys. 124 (2) (1996) 351–367, https://doi.org/10.1006/jcph. 1996.0065.
- [69] A. Toutant, B. Mathieu, O. Lebaigue, Volume-conserving mesh smoothing for front-tracking methods, Comput. Fluids 67 (2012) 16–25, https://doi.org/10.1016/i.compfluid.2012.06.019.
- [70] M.F. Thorpe, I. Jasiuk, New results in the theory of elasticity for two-dimensional composites, Proc. R. Soc. Lond. Ser. A, Math. Phys. Sci. 438 (1904) (1992) 531–544, https://doi.org/10.1098/rspa.1992.0124.